

We are IntechOpen, the world's leading publisher of Open Access books Built by scientists, for scientists

6,900

Open access books available

186,000

International authors and editors

200M

Downloads

Our authors are among the

154

Countries delivered to

TOP 1%

most cited scientists

12.2%

Contributors from top 500 universities



WEB OF SCIENCE™

Selection of our books indexed in the Book Citation Index
in Web of Science™ Core Collection (BKCI)

Interested in publishing with us?
Contact book.department@intechopen.com

Numbers displayed above are based on latest data collected.
For more information visit www.intechopen.com



Applications of Remote Sensing Instruments in Air Quality Monitoring

Chuen Meei Gan, Barry Gross,
Yong Hua Wu and Fred Moshary
*City University of New York
United States*

1. Introduction

Aerosols have become an area of intensive study both for the complex climate forcing questions that arise due to direct aerosol and indirect (aerosol–cloud) mechanisms and for air quality concerns that have arisen due to exposure to fine particulate matter. While the climate questions regarding aerosols are certainly of great importance, our focus in this chapter is to explore using remote sensing techniques the unique concerns of aerosol dynamics in an urban environment and how such understanding can ultimately be used to improve air quality modelling and forecast.

The difficulties of urban air quality forecast modelling can be grouped into two major factors. First, urban areas have extremely variable multiple pollutant emission sources and inventories of these emissions are difficult to be quantified in a common way without limitations and uncertainties (Koji & Lovei, 2001; Zhao & Frey, 2004). Second, meteorological and radiation processes which drive the aerosol generation and transport are significantly affected by complexities in the urban atmosphere coupling. In particular, urban structures can significantly affect diurnal heating processes through surface roughness mechanisms which modify wind and turbulent mechanisms as well as radiation trapping due to surfaces which absorb radiation (e.g. asphalt) and are a root cause of Urban Heat Island (UHI) mechanisms (Liu et al., 2006; Taha, 1999; Atkinson, 2003; Piringer et al., 2007; Mestayer et al. 2005). These mechanisms have a direct effect on the mixing layer which is the region that is directly affected by processes or events that occur at the earth's surface (e.g. heat transfer and turbulence). Most important for air quality applications, the planetary boundary layer (PBL) height effectively defines a total available volume for pollutant transport and dispersion (Stull, 1988) and errors in prediction of PBL dynamics will affect how the pollution forecasts are distributed. Therefore, methods that can directly explore PBL height dynamics should provide some insights into underlying difficulties observed in current air quality models are needed.

The most direct and attractive approach is so called active remote sensing techniques which can be used to range different components of the atmosphere. Once these atmospheric parameters are profiled, further analysis can then be used to estimate the PBL height. For instance, sodar and radar wind profilers monitor wind speed and by looking at statistical

fluctuations of wind speed, we can estimate the turbulent structure of the atmosphere. Since the PBL is a region where turbulent behavior dominates over the shear dynamics seen in the upper atmosphere, enhanced fluctuations in wind speed are a good indicator of PBL height. On the other hand, direct observations of the aerosol pollutants themselves are particularly valuable both as a means to monitor PBL heights and as a means of tracking the vertical structure of the aerosols directly (Kovalev & Eichinger, 2004). Ceilometers have the advantage of being eye safe and can run continuously (e.g. 24 hours / 7 days) and unattended but the signal to noise ratio (SNR) is low and vertical range is limited even if extensive temporal and spatial averaging is used. Therefore, for high mixing layers such as those in summer where convective heating causes the layer to grow, ceilometers are not suitable. In this case, the elastic lidar system (Nd:YAG laser) which has much better SNR are the only realistic choice. Unfortunately, this system is not eye safe and therefore cannot run without external observers. This makes continuous operation impractical. In addition, due to the limitations of large telescope optics, lidar signals cannot see near to surface and transmitter/receiver overlap occurs only sufficiently far from the ground (> 500 meters). This makes certain applications such as tracking surface pollutants inaccessible although merging ceilometer and lidar together may address this overlap issue. However, despite these difficulties, the optical techniques which track the aerosols directly in general outperform the turbulence based approaches as well as allow us to explore other processes so that the major focus of this chapter will be on lidar and ceilometer based techniques and their potential to address air quality questions and assess current and future air quality models.

To assess the potential of lidar based methods, we rely heavily on data and instrumentation directly available in research conducted in New York City (NYC) which is an excellent representative of the complexities of the urban environment. In particular, long term ground based multi-wavelength lidar observations have been performed at City College of New York (CCNY). A noise sensitive wavelet transform method together with additional constraints has been developed to better determine the convective boundary layer from lidar measurements (Emeis et al., 2008; Davis et al., 2000). This method is then applied over multiyear observations to assess the Weather Research and Forecast (WRF) Model (Flagg & Taylor, 2008; Gan et al., 2011). In doing these comparisons, seasonal performance issues are a particular focus (Zhang et al., 2009).

The above discussion focused on local emission and dynamics and therefore long range transport events are not considered. However, one of the strongest benefits for lidar is the direct observation of aloft layers which can affect local pollutants as well as making it difficult for satellite observations. Because of the increased extent of urban mixing layers in general; it is possible for aloft layers to mix with local emission layers. Therefore we also add a section to illustrate how this mechanism can affect PBL pollution by a case study of Aug 2007 Idaho and Montana Fires. We evaluate this smoke plume transport event using in-situ and satellite measurements combined with back-trajectory analysis (Gan et al., 2008). This section clearly illustrate why vertical information is critical in monitoring air quality and how large-scale plume transportation effect surface pollution level.

The structure of this chapter is as follows. In section 2, a brief introduction of meteorology of the PBL and the urban heat island (UHI) is given. A brief survey of current methods in

measuring air quality is discussed in section 3. Next, we give an introduction to air quality models with particular attention to those used within Weather Research and Forecast (WRF) model coupled with the Community Multiscale Air Quality (CMAQ) model environment in section 4. In section 5, descriptions of the vertical remote sensing instruments are given along with PBL height retrieval method and their advantages/disadvantages are enumerated. In section 6, discussion of the performance of air quality models in urban areas is given with special focus on the high pollution summer events. The comparisons between measurements and WRF model are presented and anomalies which may explain difficulties with CMAQ model forecasts are given. We explore the potential of remote sensing instruments to identify and quantify smoke events and their effect on local surface pollution in section 7. A summary of the chapter and overall conclusions are given in section 8.

2. Meteorology

The planetary boundary layer (PBL), also known as the mixing layer, is defined as the lowest layer of the troposphere (ranging from 100 to 3000 meters) which is directly modified by the transport processes and responds to surface forcing. Detail descriptions of PBL structure such as residual, stable and entrainment layer can be found in Stull, 1988. The diurnal variation of temperature near the earth surface is the most important driver of the PBL diurnal variability. The layer above the PBL is called the free atmosphere which shows little diurnal variation in temperature. Solar radiation and the heat capacity of the relevant surfaces provide a strong atmosphere land coupling dynamics which must be modeled properly for accurate PBL dynamics.

While modeling the PBL height dynamics is important for climate and meteorology, the important issue for air quality is that the PBL thickness also defines the total volume available for the pollutants to inhabit and be transported. For example, a high emission of local pollutants with low PBL height will result a high level pollution near the surface. This is critical since many studies have linked high surface pollution of particulate matter (PM_{2.5}) to both respiratory and pulmonary health problems (Dockery et al., 1989; Girardot, 2006). For this reason, EPA has enforced strict pollution standards as shown in Fig. 1 and the Clean Air Act (CAA).

In addition to the modifying of the temperature and wind distribution, the urban surface also affects the PBL dynamics by the heat storage of urban materials. This is commonly called the urban heat island (UHI) which describes the lack of radiative cooling of both the atmosphere and surfaces in urban areas compared to their non-urbanized surrounding during nighttime. With increasing urban development, UHI may increase in frequency and magnitude especially in summer. (Voogt, 2004; Arrau & Peña 2010)

Based on comprehensive multi-national (European) analysis (Piringer et al., 2007), the need to parameterize the affects of the UHI is crucial. For example, Mestayer et al. (2005) presents extensive measurements within city centers show that turbulent sensible heat flux is the dominant mode of heat transfer during the middle of the day but before sunrise, the largest heat transfer is limited by storage of energy within urban materials. In fact, unlike natural vegetation surfaces, the convective sensible heat flux remains positive over the diurnal cycle through release of heat stored the urban canopy. This mechanism is particularly important for air quality predictions since collapse of the urban boundary layer (UBL) due to

underestimates in the turbulent flux can result in dramatic increases in surface pollution forecasts (Doraiswamy et al., 2010). For these reasons, direct evaluation of the UBL height is important in diagnosing the performance of operational air quality models driven by high resolution meteorological forecasts.

Air Quality Index Levels of Health Concern	Numerical Value	Meaning
Good	0 to 50	Air quality is considered satisfactory, and air pollution poses little or no risk
Moderate	51 to 100	Air quality is acceptable; however, for some pollutants there may be a moderate health concern for a very small number of people who are unusually sensitive to air pollution.
Unhealthy for Sensitive Groups	101 to 150	Members of sensitive groups may experience health effects. The general public is not likely to be affected.
Unhealthy	151 to 200	Everyone may begin to experience health effects; members of sensitive groups may experience more serious health effects.
Very Unhealthy	201 to 300	Health alert: everyone may experience more serious health effects
Hazardous	301 to 500	Health warnings of emergency conditions. The entire population is more likely to be affected.

Fig. 1. EPA has assigned a specific color to each AQI category to make it easier for people to understand quickly whether air pollution is reaching unhealthy levels in their communities.

3. Current air quality monitoring efforts

3.1 AIRNow network

Current efforts to monitor fine particulate mass are based on the deployment of surface sensors which filters the particulates and can access the mass concentration directly. For example, AIRNow is an online network which is developed by EPA, NOAA, NPS and local agencies to provide real-time national air quality information daily for the public over 300 cities across the US. The air quality information is presented in a color map associated with the Air Quality Index (AQI) as shown in Fig. 1 and can be used to generate spatial maps and forecasts which are collected using either federal reference or equivalent monitoring techniques or techniques approved by the state or local agencies. The data are displayed on the website (<http://airnow.gov>) after the end of each hour so that it can be “real-time”. Therefore the data as such are not fully verified and validated through the quality assurance procedures monitoring organizations use to be officially submit and certify data on the EPA AQS (Air Quality System) even though some preliminary data quality assessments are performed. Thus, these data are not used to formulate or support regulation, guidance or

any other Agency decisions or positions as it is for the purpose of reporting the AQI. The AQI represents how clean or unhealthy of the air and what associated health effects might result.

3.2 Satellite efforts

Fire hotspots and smoke plume signatures are readily seen in satellite imagery, and many satellite sensors like GOES, MODIS (Kaufman, 1993) and TOMS (Torres et al., 2002 and Herman et al., 1997) are widely used to map the geographical distribution and aerosol transport on large scales. MODIS and TOMS (sun synchronous polar orbiting satellites) provide global coverage approximately once a day and can only provide snap-shots of large-scale aerosol spatial distribution during the time of satellite overpass, which is not very suitable for tracking and monitoring large scale aerosol events. On the other hand, although GOES (Geostationary satellite) has a single channel, unlike MODIS and TOMS, it provides coverage of the entire globe at 30 minutes intervals providing a summary of the extent of aerosol coverage, which gives a strong indication of the aerosol intensity. This gives GOES the advantage of being useful in tracking the time-history and spatial distribution of aerosol transport. Important features may sometimes go unnoticed by sun synchronous satellites, making it challenging and sometimes difficult to complete a picture. GOES can then further be used to validate features common to MODIS and OMI imagery. The goal here is to use the GOES AOD (aerosol optical depth) product to identify transport by utilizing its multi-time passes in a single day to verify features which are common in geographical area to MODIS and OMI.

While satellite measurements are critical for understanding transport and air quality prediction schemes, the lack of any vertical information of the aerosol column limits the use of these satellite measurements for air quality applications. In particular, due to the presence of possible aerosol plumes as well as poorly mixed aerosols in the PBL, connecting satellite derived AOD to surface level air quality measurements such as PM_{2.5} or PM₁₀ is very difficult. Efforts such as the IDEA product, attempt to connect satellite AOD measurements directly to PM_{2.5} using a static relationship between AOD and surface PM_{2.5} measurements.

$$PM_{2.5} = 60\tau \quad (1)$$

The coefficient in Equation 1 is statistically determined from coincident measurements from a sky radiometer and surface sampler measurements (Zhang et al., 2009). However, the cloud clearing of the sky radiometer insures that plumes are unlikely to be accounted for and all viable sky radiometer measurements occur when the PBL is the only aerosol source. Therefore, the presence of plumes will bias the surface PM_{2.5} measurements to higher values and any assessments of plume interaction with the PBL must first isolate the AOD contributions.

In particular, as we will explore fully in section 6, we unambiguously show that long term advected smoke plumes can either be transported aloft without any interaction with the PBL, or can mix with the PBL and change the air quality parameters at the surface. In both cases, lidar measurements are critical to properly apportion the PBL AOD contributions from the total column and to connect it to surface particulate matter. In particular, we show that a combination of passive and active ground instruments and satellite

measurements respectively, can provide a unique and clear picture on how PBL air quality can be affected by plumes mixing down into the PBL.

4. Air quality models and data analysis

4.1 Model description (WRF-CMAQ)

In performing comparisons to assess model performance, it is important to distinguish two different methods in running the WRF-CMAQ model. One approach is the use of retrospective analysis to better diagnose (Otte, 2008a, 2008b) the potential underlying physical parameterizations of a given model or comparisons between different models. These schemes in fact benefit from auxiliary near surface measurements which can be used to “nudge” the model during the processing. This form of data assimilation is useful as a means of identifying limitations in the model directly. This is in contrast to the natural forecast mode where the meteorological models do not benefit from additional surface data. This nudging mechanism had been applied to the MM5 model environment and had not been available within the WRF environment. However, recent implementations within WRF ARW 3.1-1 (Skamarock et al., 2008) have incorporated these observational assimilation capabilities. In particular, the nudging process ingested 3 hours surface observed data and every 6 hours upper data to adjust the annual model results.

Furthermore, it is possible to use WRF model for better observations of the differences in the PBL scheme itself since the modular structure of WRF allows different PBL parameterizations to use the same underlying surface layer schemes which in our case are the Pleim-Xiu (PX) Surface Layer Scheme (Pleim & Gilliam, 2009). In particular, two hind cast runs which are compared to our lidar and ceilometer measurements are considered whose detailed characteristics are given in Table 1. In particular, we note that our main focus is on the comparison of the Modified Blackadar (BLK) and the Asymmetric Convective Model - version 2 (ACM2) schemes are among the schemes most accurately modeling the PBL height in comparison to radiosonde and wind profiler measurements (Baker et al., 2009; Hong et al., 2006). This is also consistent with comprehensive tests made by the Environmental Protection Agency (EPA) where it was shown that the nonlocal schemes, BLK and ACM2 (PX) were better in general compared to the local schemes YSU and the Mellor-Yamada-Janjic (MYJ) PBL scheme.

On the other hand, while the nudging may improve the model error for surface temperature, humidity, and wind (although this is not an independent comparison), it may not help estimate vertical features since the upper air observation network very sparse. In addition, it must be emphasized that comparison studies in urban centers have not been made and is therefore, a major focus. During these retrospective analyses, when using the PX Land Surface Model, the pixel nearest the urban CCNY validation site is classified as 88% "Urban and Build-Up land" as defined by the USGS 24 land use category (Anderson et al., 1976). Finally, we also want to restate that our study is limited to summer where the biggest air quality issues regarding particulates in an urban environment occur and the most severe difficulties in the diurnal structure of the CMAQ air quality forecasts seem to occur (Doraiswamy et al., 2010). While summer 2007 measurements used retrospective analysis, summer 2010 forecast data were made using the MYJ PBL scheme which uses the 1.5-order (level 2.5) turbulence closure model of Mellor and Yamada (1982) to represent turbulence above the surface layer (Janjic 1990, 1994, 2001) and has become a popular model for PBL representation. (see Table 1)

Schemes	2007 WRF Run 1	2007 WRF Run 2	2010 WRF Run
PBL	Modified Blackadar	ACM2	MYJ 2.5
Surface Layer	Pleim-Xiu	Pleim-Xiu	NOAH Unified 5-layer Land-surface
Microphysics	WSM6	Morrison II	Ferrier Gridscale
Cumulus	Kain-Fritsch	Kain-Fritsch	Cumulus-Betts-Miller-Janjic
Shortwave Radiation	Dudhia	Dudhia	Lacis-Hansen
Longwave Radiation	RRTM	RRTM G	Fels-Schwartzkopf

Table 1. WRF-CMAQ Model Parametric Schemes

4.2 Data analysis for PBL heights

The first point to be made is for operational mesoscale air quality applications, the New York State Department of Environmental Conservation (NYSDEC) WRF-CMAQ runs provided to us were a final spatial resolution of 12- by 12-km grid and temporal resolution of hourly dataset. Therefore, we can expect that connecting point measurements with our lidar and ceilometers sensors may result in extensive variability. However, we note that since the PBL measurements from WRF are per hour, we are able to reduce much of the variability in our point measurements by similar one hour averaging of the lidar PBL retrievals. Due to natural wind flow, the one hour averages should be reasonably representative of the 12 km spatial footprint. To improve the data matchup quality, we also introduce the following filters into the lidar matchups.

Filter 1: Only cloud free cases are considered. This is in fact a limitation of the lidar measurements since operation under cloudy conditions can result in strong backscatter signals that would often saturate the detector. Since we are ultimately concerned with cases where pollution exceedence is of major concern and to avoid local coastal contamination issues, we remove from our comparisons all sea-breeze cases identified through wind data from Hybrid Single Particle Lagrangian Integrated Trajectory (HYSPLIT) Model.

Filter 2: We restrict comparisons to cases where at least five PBL measurements are made within the hour and the standard deviation is less than 20% of the mean. This limits comparisons to cases where temporal homogeneity is reasonably met.

4.3 Data analysis for PM_{2.5}

While our first concern is the PBL heights, we also look to assess the performance of the WRF driven CMAQ forecast predictions. As mentioned earlier, the CMAQ model performance for summer conditions in urban conditions results in strong overestimating pollution spikes which are not in agreement with the AIRNow TEOM measurements.

Particulate size distributions in CMAQ are represented as the superposition of three lognormal subdistributions, called modes, including the aitken mode (i-mode), accumulation mode (j-mode), and coarse mode (c-mode). In general, a large number of species with different optical and density properties are represented but all particles are assumed to share the same size distribution. In this study, we estimate the PM_{2.5} from the CMAQ output by simply summing the aitken and accumulation mode or (i+j) method (EPA, 1999a, 1999b; Jiang et al., 2006). In comparing with the TEOM measurements, we use three sites within the 12km area (see Table 2) and filter the cases to those in which the standard deviation of the three sites is < 20 % of the mean.

Site Name	Latitude	Longitude
CCNY	40.81976 N	-73.94825 W
Manhattanville PO	40.81133 N	-73.95321 W
IS 52	40.81618 N	-73.90200 W

Table 2. TEOM Stations Locations

5. Instrumentations and methodology

5.1 Lidar

An elastic lidar with three wavelengths (355 nm, 532 nm and 1064 nm) is operated year round in CCNY (40.8N, 73.9W). Measurement at wavelength 1064nm is mainly used in this study as this channel has minimum contribution from molecular scattering and is better for aerosol observation by increasing the backscatter contrast between the PBL and free troposphere layers. More details about lidar specifications and system configuration can be found in Wu et al., 2009.

The lidar return signal is based on the scattering of the laser transmitted energy by atmospheric particles including aerosol, dust and molecules. The instantaneous magnitude of the return signal provides information on the backscatter properties of the atmosphere at a certain height determined by the time delay of the pulse echo. While processing the raw lidar data, we must include the fact that the atmosphere attenuates the signal both before and after hitting the backscattering target. To account for this, the instantaneous return signal strength is given by the basic LIDAR equation:

$$P_r(z) = E_o \cdot \frac{c\Delta t}{2} \cdot \frac{A}{z^2} \cdot \beta(z) \cdot e^{-2 \int_{z_1}^{z_2} \sigma(z') dz'} \quad (2)$$

where $P_r(z)$ is the instantaneous power received from distance z [Watt], E_o is the effective pulse energy (include all optics attenuation) [Joule=Watt-second], c is the speed of light [meter per second], Δt is the laser pulse width [second], A is the receiver aperture area [meter²], z is the distance between system and target [meter], $\beta(z)$ is the volume backscatter coefficient at distance z [per meter-steradian] and the exponential term is the two-way atmospheric transmittance, which accounts for the attenuation of transmitted and backscattered power by extinction at various distances (z') between the transceiver and target.

The PBL contains greater aerosol concentration because the aerosols are trapped in the PBL by a potential temperature inversion. Therefore, the backscatter signal strength is dramatically reduced when it transits from the PBL into the free troposphere. This sharp change of signal is used to estimate the PBL height. These changes in backscatter signal caused by varying aerosol concentration provide a very powerful tool for remotely observing the two-dimensional structure of the PBL. In general, the PBL is characterized by intense mixing in a statically unstable situation where thermals of warm air rise from the ground. The PBL reaches its maximum depth in late afternoon. It grows by entraining, or mixing down into it, the less turbulent air from above. The resulting turbulence tends to mix heat, moisture, pollutants and momentum uniformly in the vertical. (Stull, 1988; Kovalev & Eichinger, 2004; Brooks, 2003; Davis et al., 2000)

5.2 Ceilometer

Another remote sensing instrument that is used in this study is a ceilometer (model CL31) which is manufactured by Vaisala. This instrument is a device that is originally designed to determine the height of a cloud base. Due to the higher backscatter signal of a cloud, the pulse powers are dramatically less and therefore can be made eye-safe but works on the same principle as lidar system. Furthermore, unlike the lidar transmitter which is not eye-safe, the ceilometer utilizes a single NIR (Near Infra Red) channel at 910 nm. While designed for cloud detection, ceilometers can also be used to measure the aerosol concentration within the atmosphere (Eresmaa et al., 2006; Haji et al., 2009). However, it is also clear that the low signal pulse power will result in higher noise and significant temporal and spatial averaging would need to be applied to bring the noise contamination down to acceptable levels. Besides, the limitation of this instrument is unable to observe PBL height that is higher than 1.2 km where the noise is dominant.

5.3 Wavelet covariance transform method

From extended studies of the performance of the available lidar methods applied to a large set of lidar observations, the wavelet covariance transform (WCT) method has been shown to be the most robust technique for an automated PBL height detection (Davis et al, 2000; Brooks, 2003; Baar et al. 2008). This method is intuitive and is based on scanning the backscatter profile with a localized impulse function and maximizing the covariance between the backscatter profile and the impulse function. While many possible wavelet shapes are possible, we find that a step function Haar wavelet defined as below can be used.

$$\begin{aligned}
 &1: \quad b - \frac{a}{2} \leq z \leq b \\
 h\left(\frac{z-b}{a}\right) &= -1: \quad b \leq z \leq b + \frac{a}{2} \\
 &0: \quad \text{elsewhere}
 \end{aligned} \tag{3}$$

where z is the profile height and a and b describe the width and translation of the function, respectively. The covariance (Gamage & Hagelberg, 1993) is simply the convolution or localized transform, $W_f(a,b)$, of the Haar function with the lidar backscatter profile.

$$W_f(a,b) = a^{-1} \int_{z_b}^{z_t} B(z) h\left(\frac{z-b}{a}\right) dz \tag{4}$$

where z_b and z_t are the bottom and top altitudes in the lidar backscatter profile, and $B(z)$ is the lidar backscatter as a function of altitude, z . The locations of these maxima and minima, b_i^{max} and b_i^{min} , and the associated values of the covariance transform, $W_f(a_{max}, b_i^{max})$ and $W_f(a_{max}, b_i^{min})$, are the locations and relative strength of step like boundaries in the lidar backscatter profile, $B(z)$. The index i refers to the case of multiple local minima or maxima. For clear conditions, $W_f(a,b)$ takes a clear local maximum at the PBL height because of the high backscatter values in the mixing layer and significantly lower backscatter values in the free atmosphere (Fig. 2).

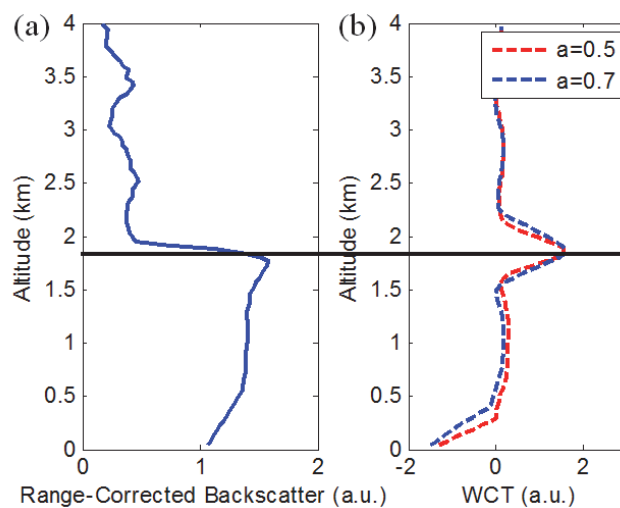


Fig. 2. (a) Single Lidar signal (log scale) profile (b) Resulting wavelet covariance transform.

However, when strong residual or plume layers occur, $W_f(a,b)$ will have multiple local minima and maxima as shown in Fig. 3 (a). These multiples maxima confuse the algorithm making it difficult to extract a unique PBL height. For example, Fig. 3 (b) illustrates 4 hours lidar measurements where an aloft plume occurs in the morning. The backscatter from the plume is higher than the backscatter from the PBL which gives the wrong estimation of PBL height. This renders the selection of the correct PBL height ambiguous and it is this ambiguity that needs to be addressed for better model validation.

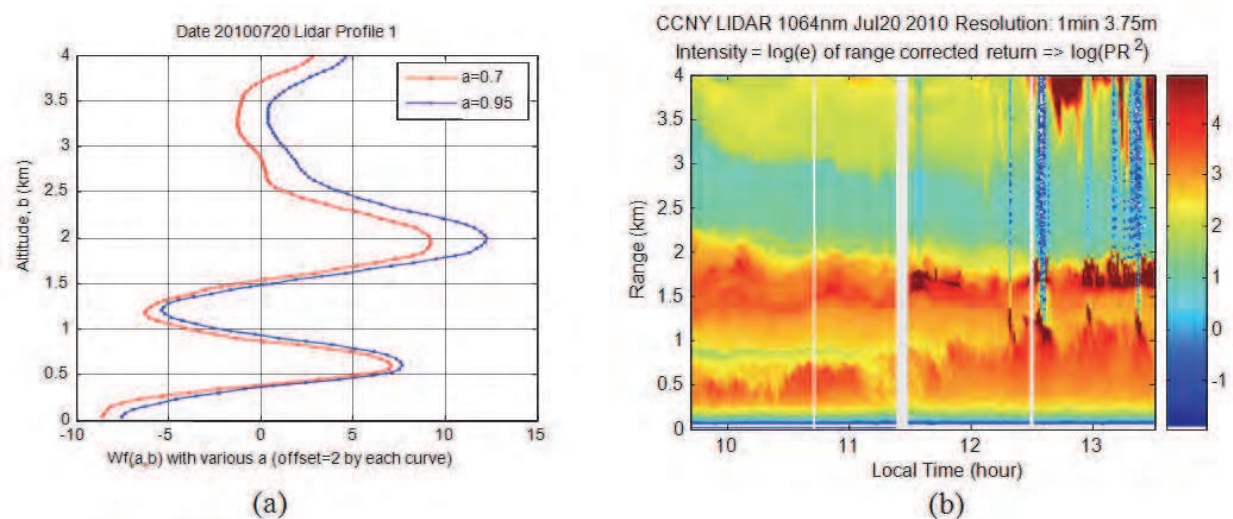


Fig. 3. (a) Single lidar WCT profile (b) Lidar measurements on Jul 10, 2010.

To account for the different structures expected in the PBL height, we separate the lidar profiles into classes. The “transition” class occurs between 8:00-12:00 EST and 18:00-22:00 EST when the PBL is growing / collapsing and residual layers are present growing, while the mature PBL class extends from 12:00-18:00 EST. In order to decrease the noise level and smooth the atmosphere transition, a sliding spatial and temporal averaging is applied to the lidar backscatter dataset. In this study, the averaging temporal interval Δt is 20 minutes with a sliding window of 10 minutes while the averaging spatial interval Δz is 80 meters with a

sliding window of 40 meters. The temporal resolution is 10 minutes and spatial resolution is 40 meters. Since the PBL height predicted by the WRF model is hourly, 10 minutes temporal resolution is sufficient for comparison. When making final comparisons however with the WRF outputs, the 10 minutes retrievals are further averaged to 1 hour. To better separate the convective layer from the residual or plume layer, we apply a few modifications that will be briefly discussed below.

Our first modification is applying cloud screening to the dataset before WCT. Clouds are characterized by a steep increase of the range-corrected lidar signal at the cloud base followed by a strong decrease of the signal with increasing cloud penetration depth. From these properties, the use of the WCT and together with a minimum backscatter threshold is sufficient to easily identify cloud pixels in the lidar profile. For such marked cases, no PBL height is provided.

Furthermore, the selection of an appropriate spatial resolution a is the main challenge for a successful retrieval of the PBL height. For rather small values of a , signal noise dominates the vertical profile of W_f masking the maxima that defines the PBL top. On the other hand, large value of a may fail to resolve the PBL height when further aerosol layers are present in the lower free troposphere. In general, we found that a smaller a (0.5 km) is needed during the transition regime while a larger a (0.7 km) is optimum for the afternoon time dataset. The larger value allows us to balance the effects of lower SNR due to the higher altitude where the signal strength is degraded with the reduction of vertical structure of the PBL due to turbulent mixing during this period

In addition, to isolate the convective growth layer from the residual layer, we make use of general trends (e.g. climatology) in the PBL searching range to limit the PBL height retrieval. For example, we restrict the PBL searching range to 1 km in the morning and night period while a range from 1 to 3.5 km is used for the afternoon period. The restriction in morning is necessary since the residual layer is often very deep from the previous day.

Finally, the PBL height determined by the algorithm is checked for continuity. On a running scale, a given interior point is compared to its adjacent points and if it is outside a range (e.g. ± 250 meters with spatial resolution of 40 meters and temporal resolution of 10 minutes) on both sides, it is discarded. If only one side is outside the range, a mean value of both points will be calculated. This scheme is iterated until no further changes occur. This reduces the number of false hits caused by noise or other layers such as residual layer, plume layer and internal turbulence.

6. Discussions

6.1 PBL statistic variations in NYC

In order to have a general idea of the PBL temporal dynamics in an urban area such as NYC, we overlay the PBL trend grouped by seasons. Due to the weather and human factors, the lidar observations are normally limited from 10:00 to 18:00. Therefore, the results as shown in Fig. 4 (a-b) only illustrate the daytime trend. Table 3 summarizes the number of observation days and averaged maximum PBL height that occur during daytime for each month. The most important observations is the high PBL height (2-2.5 km in summer) as compared to winter seasonal trends (1-1.5 km in winter) (e.g. January, February and December). In addition to the general increase of the maximum PBL height, the diurnal increase from morning through late afternoon is much more dramatic and indicative of the surface heating process in general during the summer and spring.

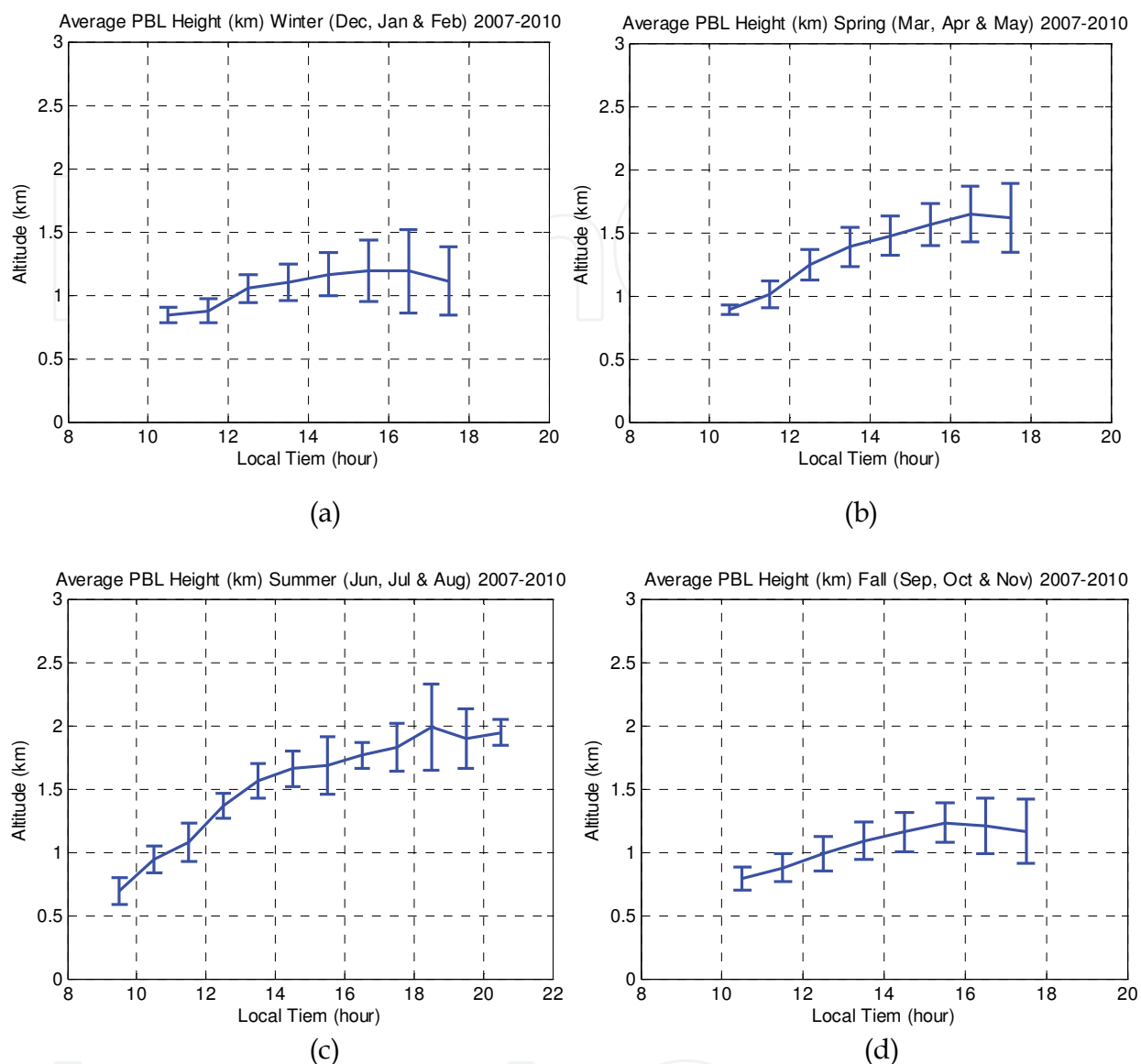


Fig. 4. Monthly PBL trend average over 4 years (2007-2010).

Month	1	2	3	4	5	6	7	8	9	10	11	12
No. Days	12	16	29	28	30	16	32	24	26	25	22	11
Max Height (km)	0.99	1.30	1.88	1.78	1.80	2.05	2.23	2.02	2.21	1.11	1.18	1.48

Table 3. Summary of number of observation days and maximum PBL height.

6.2 Assessment of model PBL height retrieval

The main results when comparing both the BLK and ACM2 data are given in Fig. 5 (a-b). First, we note the BLK has somewhat slightly better correlation ($R=0.87$) than the ACM2 scheme ($R=0.84$) although both schemes seem to result in statistically significant

overestimations of the PBL height. However, as seen in the histogram analysis of Fig. 6, the bias of the BLK scheme is somewhat smaller than that observed in the ACM2 scheme with a mean bias of $m=180$ meters for BLK and $m=340$ meters for the ACM2 scheme. On the other hand, the fluctuation of the deviation is quite high with the std for the BLK scheme about $\sigma_{\text{BLK}}=300$ meters while the ACM2 schemes standard deviation is $\sigma_{\text{ACM2}}=280$ meters. Keeping in mind that the lidar based methods matched against meteorologically based methods such as the parcel method show no appreciable bias and average deviations between on the order ± 200 meter (Hennemuth & Lammert, 2006), we believe the model biases are significant and there is room for more model development. Still, the results illustrate that at least for ACM2, the over bias is significant and all things considered, the BLK scheme performs best under the study period.

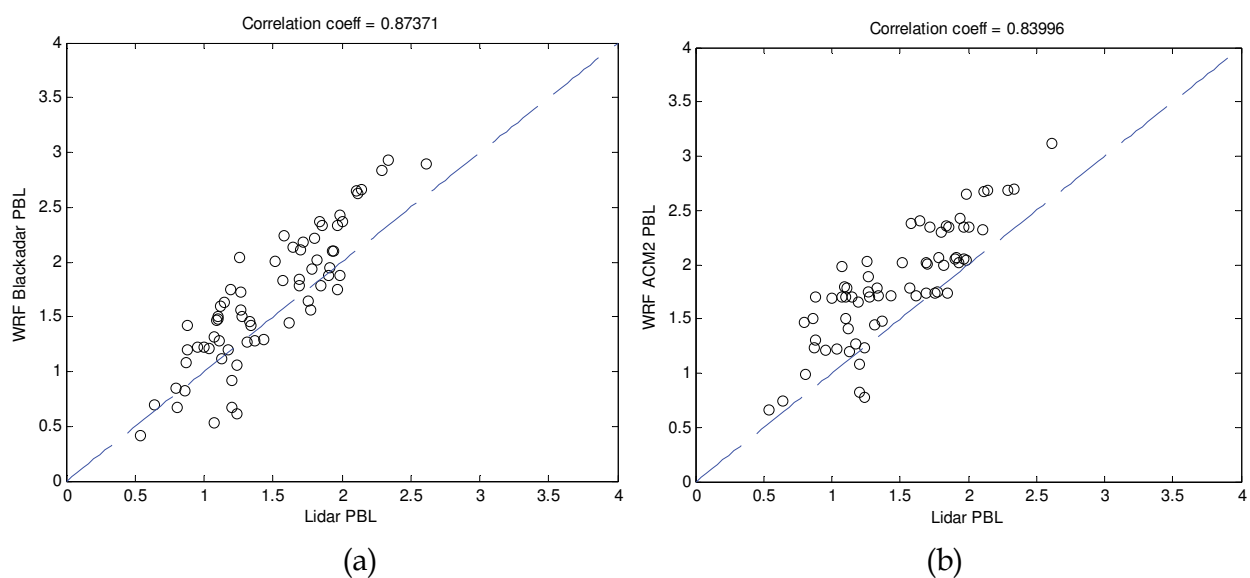


Fig. 5. WRF versus Lidar PBL heights in unit km (a) Blackadar (b) ACM2.

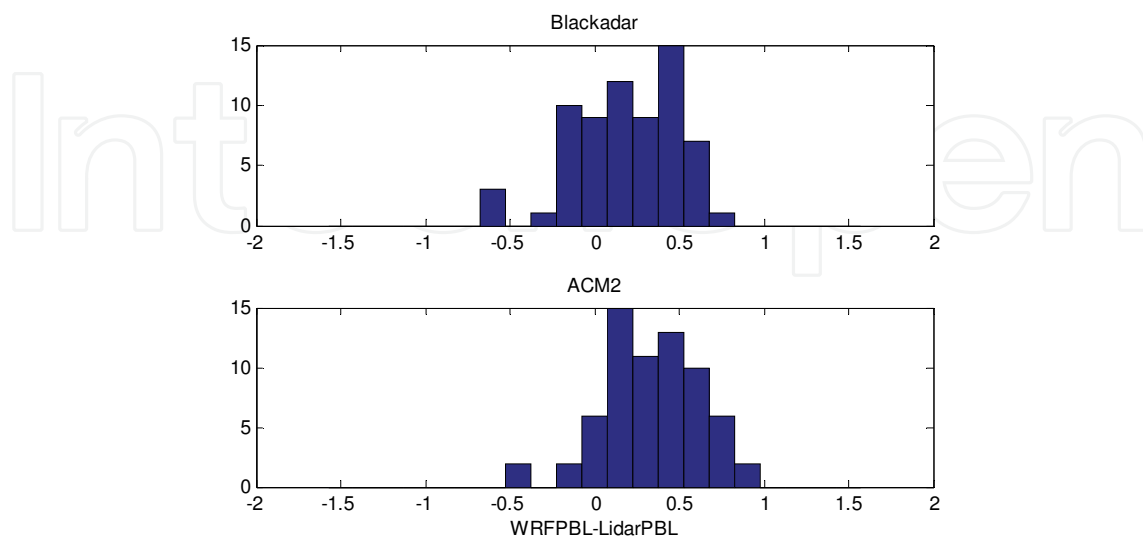


Fig. 6. Statistics of PBL height model versus measurement errors (WRF PBL - Lidar PBL in unit km) summer 2007 (a) Blackadar (b) ACM2.

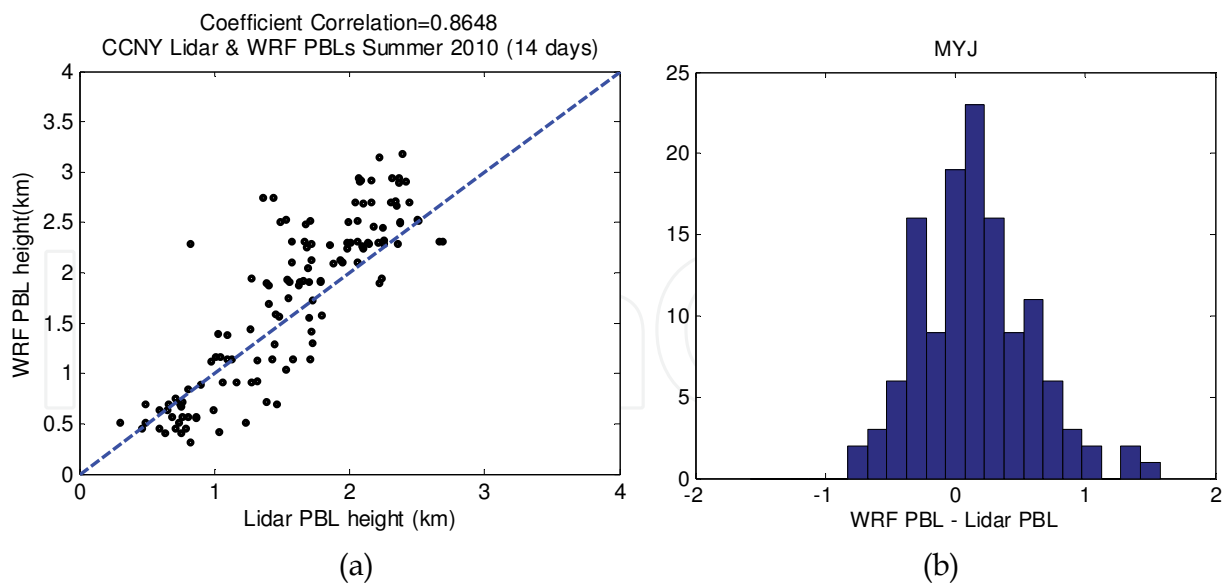


Fig. 7. (a) Linear regression of WRF PBL height with lidar derived PBL height for selected 14 days on June, July and August, 2010 (b) Statistics of PBL height model versus measurement errors (WRF PBL – Lidar PBL in unit km) summer 2010.

The results for the 2010 PBL height comparisons using the MYJ scheme in forecast mode are given in Fig. 7 (a). We note however that even though the correlation is comparably high ($R \sim 0.86$) to the 2007 hind cast data, the fluctuations for the 2010 forecast data is much larger as seen in the histogram data as shown in Fig. 7 (b) with a standard deviation $\sigma_{MYJ} \sim 550$ meters in comparison to $\sigma_{BLK} \sim 320$ meters and $\sigma_{ACM2} \sim 280$ meters. This is consistent with the fact that forecast uncertainties are expected to significantly increase the fluctuations of all dynamical parameters.

6.3 Assessment of CMAQ PM2.5

In looking at the performance of CMAQ as illustrated in Fig. 8, a strong diurnal spike behavior is observed in the CMAQ surface layer PM2.5 which is not seen in the TEOM measurements. The direct source of this over bias is not clear with possible contributing factors being unrealistic gradients in the PM2.5 vertical profiles or overestimation in the primary emission associated with urban rush hour traffic (Doraiswamy et al., 2010). However, the use of ceilometer backscatter profile data can be used to explore how realistically, the primary emissions are distributed vertically. Before doing this, it is useful to illustrate indirectly that vertical distribution of PM2.5 is at least partially a factor that must be taken into account seriously. In Fig. 9, we plot for the summer 2007 case, the linear correlation coefficient binned by hour between the TEOM PM2.5 measurements and the path averaged PM2.5 mass from the CMAQ model for different vertical height levels. Most dramatic is the enhancement of the correlation for the pre-sunrise particulate matter emission case when the altitude is large. This illustrates that to some extent, the primary emission is not the dominant problem and that these emissions are in practice being more evenly distributed in the UBL. On the other hand, we see a complete change once sufficient heating has taken place during the day. In this case, the particulate matter mass in the CMAQ model is better mixed in agreement to observations and the best correlation should occur when the CMAQ particulates is closest to the surface.

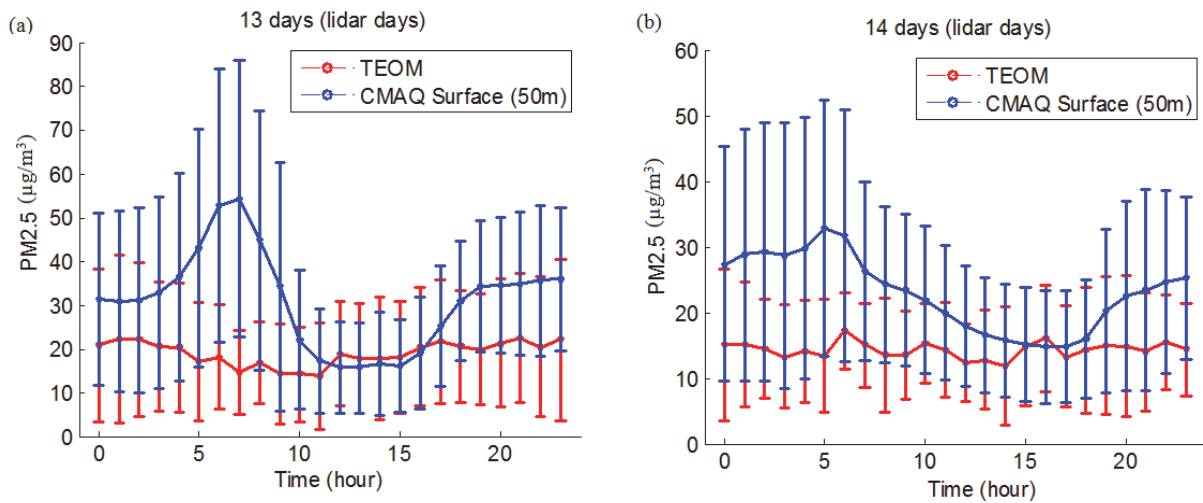


Fig. 8. Summer averaged PM2.5 mass concentration ($\mu\text{g}/\text{m}^3$) diurnal cycle comparison of CMAQ and TEOM. (a) Summer 2007, (b) Summer 2010.

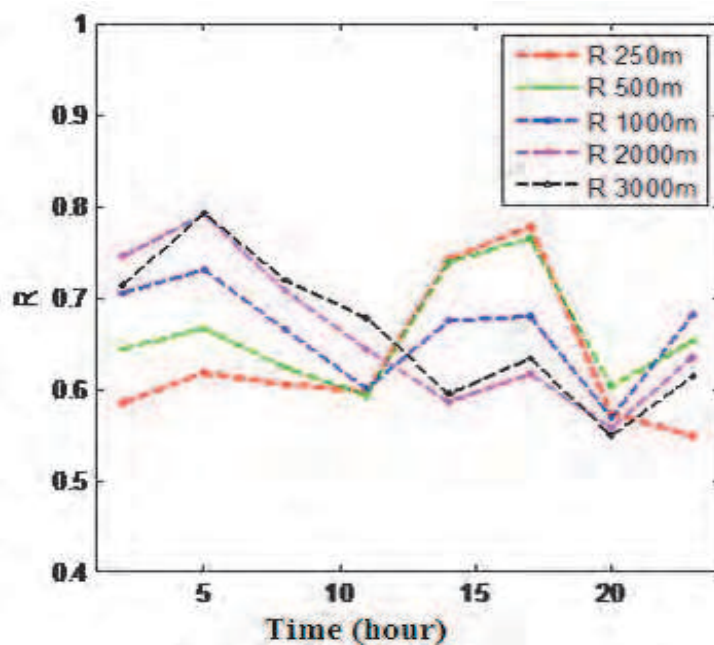


Fig. 9. Linear correlation coefficient binned by hour between the TEOM PM2.5 Summer 2007 measurements and the path averaged PM2.5 mass from the CMAQ model for different vertical height levels. (R: correlation coefficient; 250 meters: path average from the surface to 250 meters altitude)

For a more direct comparison, we plot in Fig. 10 path averaged CMAQ PM2.5 and the ceilometer backscatter over the diurnal cycle for different altitude ranges. In panel (a), the results reemphasize how the CMAQ PM2.5 distribution is compressed near the surface during the morning spike anomaly. In fact, as the altitude increases, the PM2.5 diurnal distribution becomes peaked during mid-day and evidence of the spike behavior is removed. On the other hand, the ceilometers path averaged backscatter in panel (b) does

not observe these pollutant spikes even at the lowest vertical bins. While a small increase is seen in the ceilometer backscatter relative to mid day, the contrast between morning and mid-day is much smaller with a contrast coefficient $C(X) = (X_{\max} - X_{\min}) / (X_{\max} + X_{\min})$ of approximately 12% compared to ~50% for the CMAQ near surface measurements. In addition, the ceilometer contrast is clearly much more in line with the TEOM measurements. It is also interesting to see that as the height of the ceilometer path increases, we recover the general diurnal trend seen in the CMAQ data retrievals.

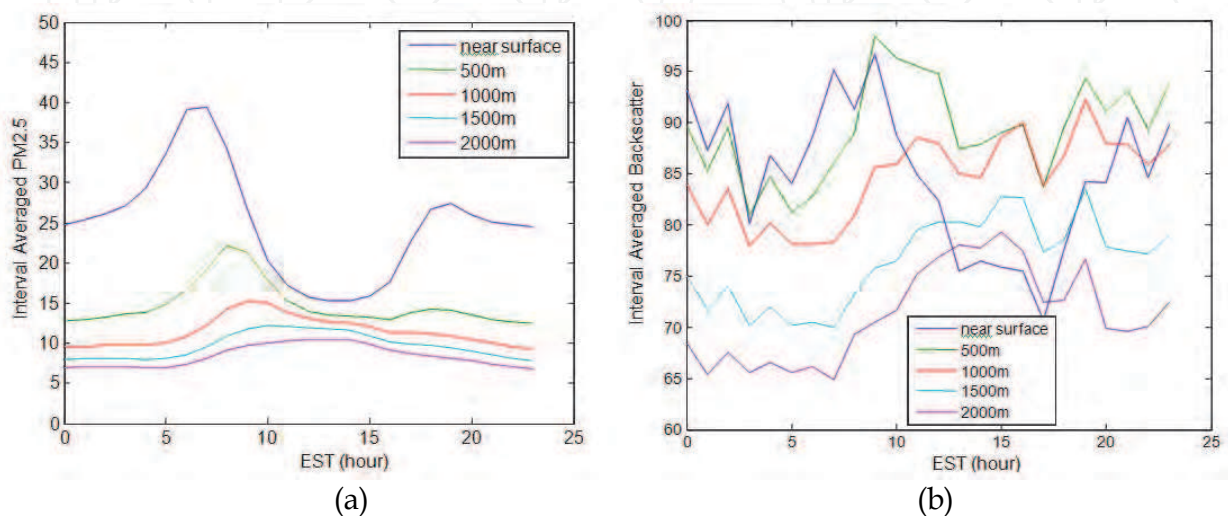


Fig. 10. Cumulative path averaged parameters for different altitude ranges over the diurnal cycle (a) CMAQ $PM_{2.5}$ ($\mu\text{g}/\text{m}^3$) (b) Un-calibrated ceilometer backscatter ($10^{-9} \text{ m}^{-1} \text{ sr}^{-1}$).

Further evidence that boundary layer mechanisms giving rise to problems with the near surface $PM_{2.5}$ estimates can be seen by inter-comparing the summer 2007 and 2010 CMAQ predictions. In Fig. 11, the 3-dimensional structure of the CMAQ $PM_{2.5}$ outputs are compared. For convenience, the different PBL height retrievals are superimposed. The most important observation is that the summer 2010 mixing layer heights are significantly larger on average for summer 2010 during the sunrise/sunset periods. For the 2007 data, the extremely compressed PBL clearly tends on average to trap the primary emissions not letting them vent upwards. Since the emission inventories are not expected to be significantly different when averaged over seasonal scales, the different PBL height behavior is clearly the dominant mechanism. The difference in PBL height is directly observed in Fig. 12 where the different PBL height retrievals are plotted. Besides the significant growth of the nocturnal PBL, we note a significant increase in the magnitude and persistence of the PBL profile.

Finally, it is important to remember that when we compared the vertical structure of the CMAQ against the ceilometers in Fig. 9-10, we found that the strong surface emission behavior in the diurnal pattern predicted by CMAQ within the first 500 meters of the surface are not seen in the ceilometer data. However, it may be argued that since we are matching $PM_{2.5}$ to optical backscatter, there may be significant problems in the comparison. Although we argued that this should not be a significant issue since the TEOM-Ceilometer regression has high correlations in the first 500 meters, it is useful to consider a more direct matchup where we use the CMAQ extinction variable based on semi-empirical parameterization connecting the CMAQ component masses to optical extinction (Malm et

al., 1994). In Fig. 13 (a), the averaged optical extinction data is displayed and in Fig. 13 (b), the accompanying seasonally averaged relative humidity (RH). The first point is that the CMAQ extinction parameter has the same near surface behavior with the PM_{2.5} mass so that it is not unreasonable to diagnose the CMAQ PM_{2.5} with the lidar and ceilometer backscatter. In this direction, it is clear that CMAQ primary emissions are not properly being distributed vertically. On the other hand, enhanced extinction is seen in the CMAQ retrievals in the upper atmosphere but when compared to the WRF RH profile is a direct consequence of the enhanced scattering due to hygroscopic humidification. This enhanced backscatter does in fact exist in our lidar images where increased humidity at the top of the PBL is often accompanied by enhanced RH due to temperature inversion and an increase of hazy layers capping the PBL in the afternoon but occurs too high to be of interest in our ceilometer retrievals.

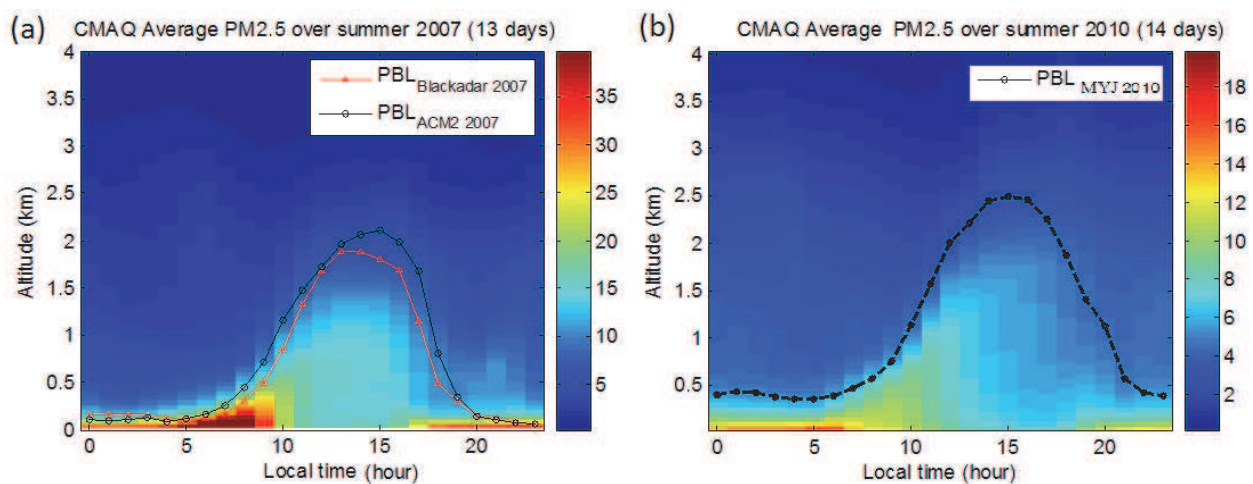


Fig. 11. The 3-Dimensional structure of the CMAQ predicted PM_{2.5} mass concentration ($\mu\text{g}/\text{m}^3$) (a) Summer 2007 (b) Summer 2010.

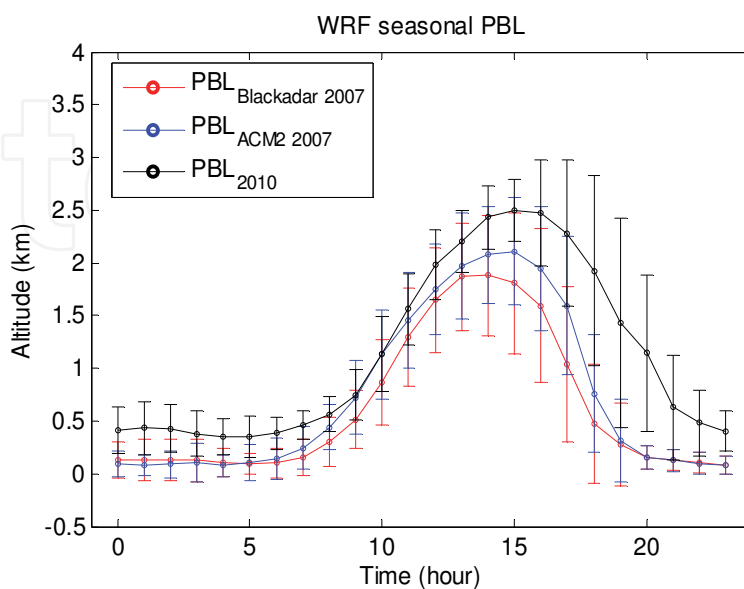


Fig. 12. Diurnal Average of PBL height retrievals for different schemes.

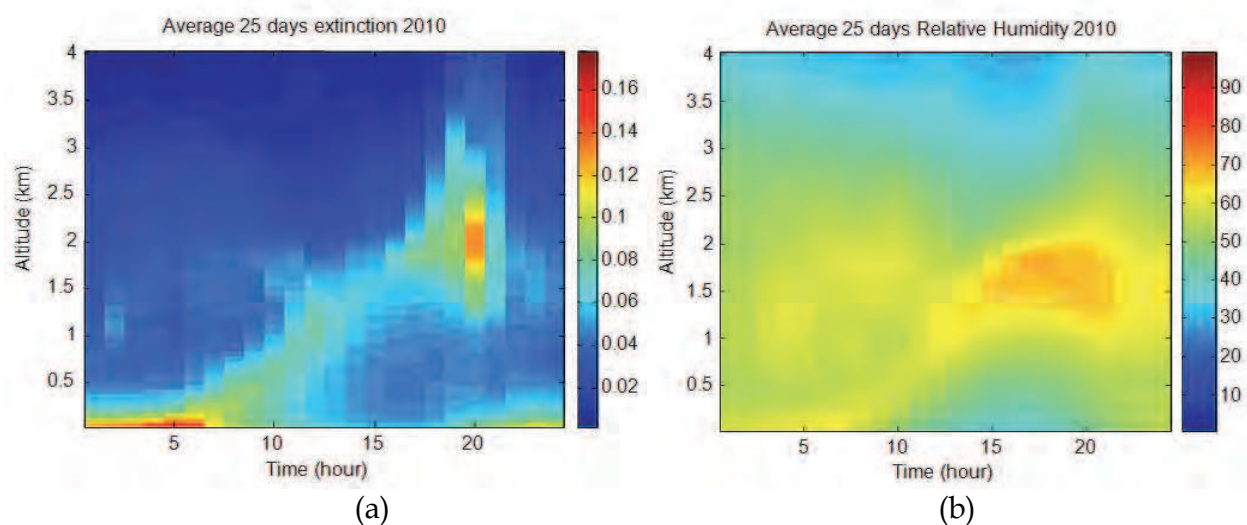


Fig. 13. (a) Optical extinction (km^{-1}) at wavelength 550 nm based on the MALM parameterization within the CMAQ product (b) Simultaneous WRF RH (percent) retrievals.

7. Case study – august 2007 Idaho and Montana fires

In section 3, we briefly mentioned satellite based approaches to measure pollutants focusing on MODIS AOD as a proxy for PM_{2.5}. However, this approach does not work if aloft plumes are present since they modify the column AOD. These plumes not only affect the PM_{2.5} retrieval but also can physically interact with the PBL and change the surface PM_{2.5} concentrations.

7.1 Plume identification using polar satellites

To determine the nature of the aerosol plumes, a number of more advanced multi-spectral satellites including OMI, POLDER, and MODIS to name a few have the added capability of limited aerosol classification. In order to illustrate the phenomenon, we choose the mid August (Aug) 2007 fires, which were continuously burning across Idaho and Montana with columns of thick smoke transported eastwards across North America, affecting much of the United States. Although it was assumed that this event significantly affected air quality in the north east, observations from satellites are not conclusive and in fact during the plume transport, surface samplers often showed low pollutant levels. The advanced warning provided by the satellites was crucial to ensuring that this transport event was captured by the CCNY lidar as well as other lidars from the Micro-pulse Lidar Network (MPLNET). However, the column AOD does not directly determine the surface pollution when plumes are present since the aloft plumes cannot be differentiated from the satellite measurements. Therefore, lidar (ground based or space based) must be employed to quantify the AOD in the plume and thereby correct for the plume contribution to the satellite AOD.

As an example of how we could do this, we look at a special case of heavy smoke plumes from Idaho-Montana. The plumes were initially transported as high altitude lofted layers which was observed by the CCNY lidar system (40.8N, 73.9W) over two days and was subsequently observed to mix with the late afternoon PBL. The source of the plume is shown in Fig. 14 (a) as fire hot spots and smoke signatures captured by MODIS onboard the Aqua satellite on Aug 13. By Aug 14 and 15, the smoke plumes began to canvas the North Eastern United States as seen

in Fig. 14 (b) and were visually identifiable from the quick view imagery, as well as through the large AOD measurements seen from the GOES and MODIS satellites.

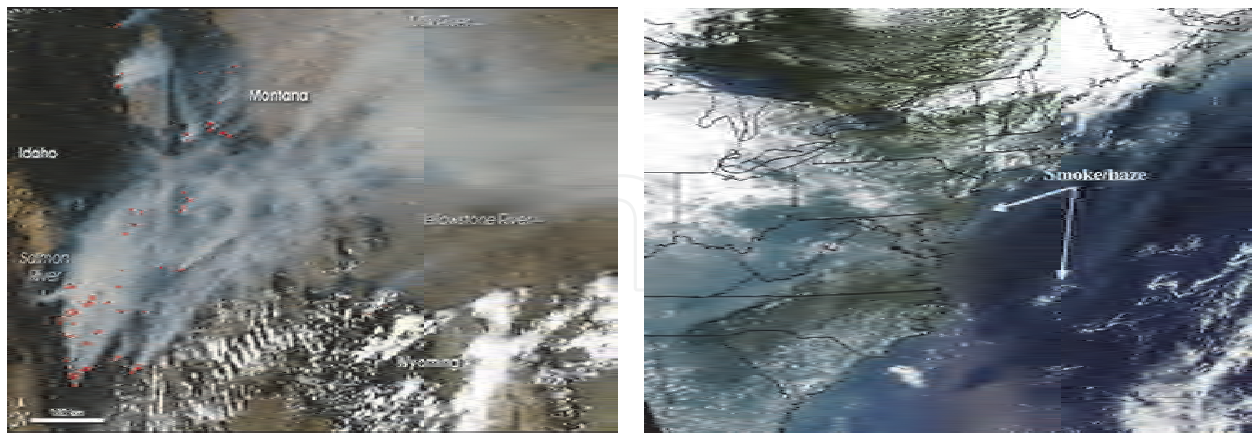


Fig. 14. (a) Images showing smoke and fires area (Montana and Idaho) captures by MODIS aboard Aqua satellite on Aug 13, 2007. This image of the area was captured by MODIS on NASA's Aqua satellite at 2:00 p.m. local time (U.S. Mountain Daylight Time). Locations where that sensor detected active fires are highlighted in red. (b) MODIS Terra close-up view of the smoke and haze over the Great Lakes and the northeastern United States on Aug 15, 2007 at 1625 UTC.

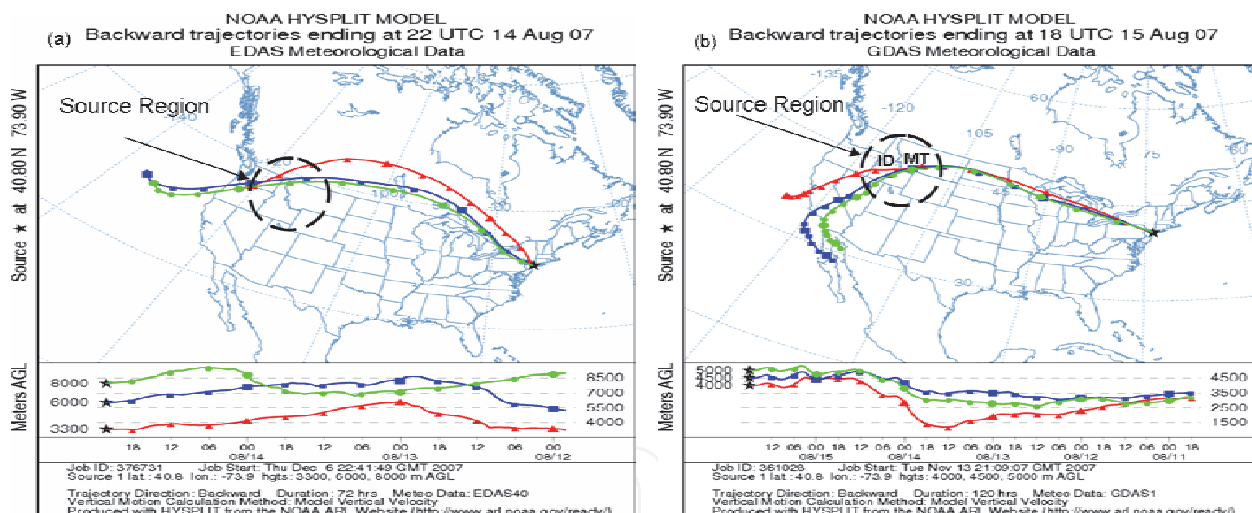


Fig. 15. HYSPLIT 5-day backward trajectory analysis ending at (a) 22:00 UTC on Aug 14 at three altitudes between 3 and 8 km and (b) 18:00 UTC on Aug 15, 2007 between 4 and 5 km.

Modeled backward trajectories from HYSPLIT (DeMott et al., 2003; Jorba et al., 2004; Hondula et al., 2009) provide a means to identification of the source region and the transport patterns of the air parcels at varying altitudes as specified by lidar observations. In Fig. 15, we show the back-trajectory of the air parcels over 120 hours from CCNY for Aug 14 and 15, illustrating the horizontal and vertical motion of the air mass. The trajectory results clearly show the air mass interacting with the aloft layers from the Idaho and Montana forest fire regions. This backward mode then allowed us to run HYSPLIT in prediction mode, which can then be compared to observations. Running the smoke forecast tool produced by NOAA Air Resource Laboratory (ARL) using the HYSPLIT dispersion model with the MODIS aerosol loadings shows how well

the model performs. In particular, MODIS aerosol retrieval continuously shows high aerosol optical depth over the source region over all three days in Fig. 16 (b, d, f). However, we can see that on Aug 13 as shown in Fig. 16 (b), very low aerosol loadings over the NYC region occur, implying that the smoke plumes had not made its way to this area as yet, as predicted

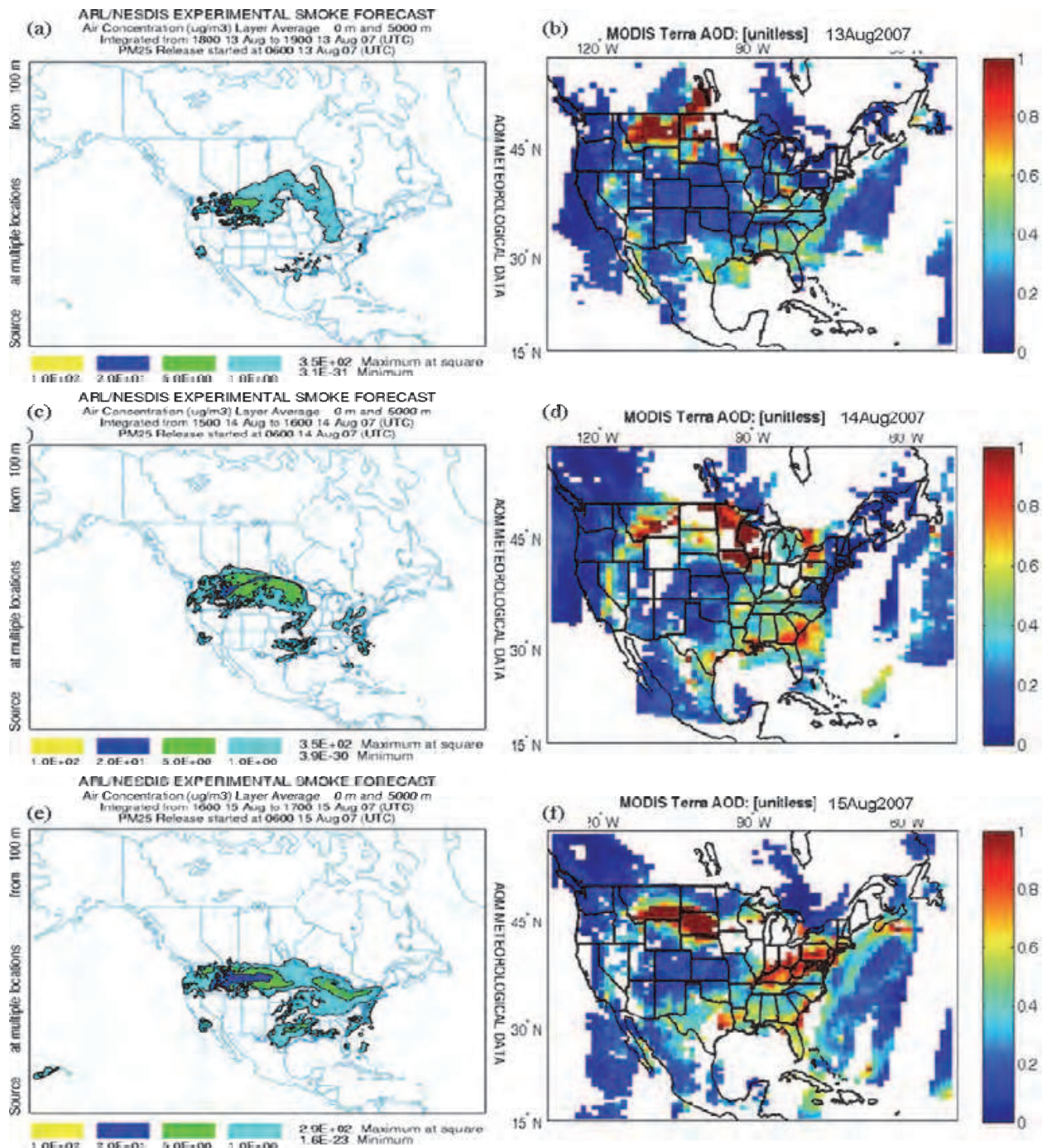


Fig. 16. MODIS Terra AOD at 550 nm on (b) Aug 13, (d) Aug 14, and (f) Aug 15, 2007. NOAA ARL smoke forecast for (a) Aug 13, (c) Aug 14, and (e) Aug 15, 2007. The smoke forecasts are 1-hour average output maps of primary PM_{2.5} air concentrations between the ground and 3 km. Smoke Forecast Model courtesy of NOAA's Air Resource Laboratory using the HYSPLIT Dispersion Model.

by the model. On the other hand, we can see much higher aerosol loading on Aug 14 and 15 as shown in Fig. 16 (d and f), which is consistent with the CCNY lidar observations and model predictions. The quality of the predictions is also seen in the timing of the plume front. A more careful examination of the observations and model predictions show that by 1600 UTC, the plumes were first making their way into central New York and did not make it into the NYC Area. This is consistent with the timing of the plumes observed from the CCNY lidar system where the first plumes were seen at 2000 UTC.

To further identify the nature of the plume coefficient as well as the underlying aerosol environment, we plot in Fig. 17 the angstrom coefficient derived from MODIS AOD. The Angstrom exponent α quantifies the slope of the wavelength dependence of the optical depth and is an indicator of the size of the atmospheric particles. In particular, when the Angstrom exponent is larger than one, fine mode aerosols dominate the column, while for Angstrom exponents less than one; coarse mode aerosols dominate the column [Kaufman, 1993]. In particular, we note that the plume as well as the background aerosol angstrom coefficient is quite high, which is indicative of highly concentrated fine mode aerosols. However, to identify the aerosols as biomass burning, we need to obtain information on the absorbing nature of the aerosols, which is beyond the capabilities of MODIS. Therefore, we utilize the UV (ultraviolet) aerosol measurements from AURA's OMI sensor, which allows for the determination of the absorbing index (AI) parameter known for its strong indications of biomass burning. These results are reported in the next section.

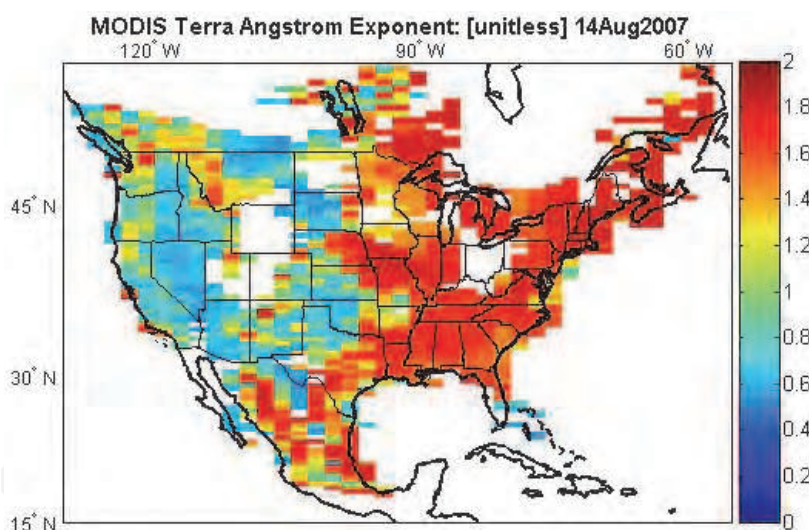


Fig. 17. Mosaic of Angstrom Exponents over North America derived from MODIS on Aug 14, 2007.

The Aura OMI instrument can differentiate UV-absorbing aerosols such as dust and biomass burning from the weakly absorbing aerosols and clouds (Braak et al. 2007). Absorbing and non-absorbing aerosols are separated based on the UV aerosol index, which is positive for absorbing (e.g. dust) and negative for non-absorbing aerosols (Torres et al. 2002). Since we have already eliminated dust due to the MODIS observed high angstrom coefficient, a high AI coefficient is a good indicator of biomass burning. In Fig. 18 (a), we see the strong biomass signature of the fire source. By Aug 14, the biomass plume had been transported to the northeast US. Although the AI is slightly smaller, the biomass signature is still quite clear. By Aug 15, the plumes are observed to be heading out to sea and mixing

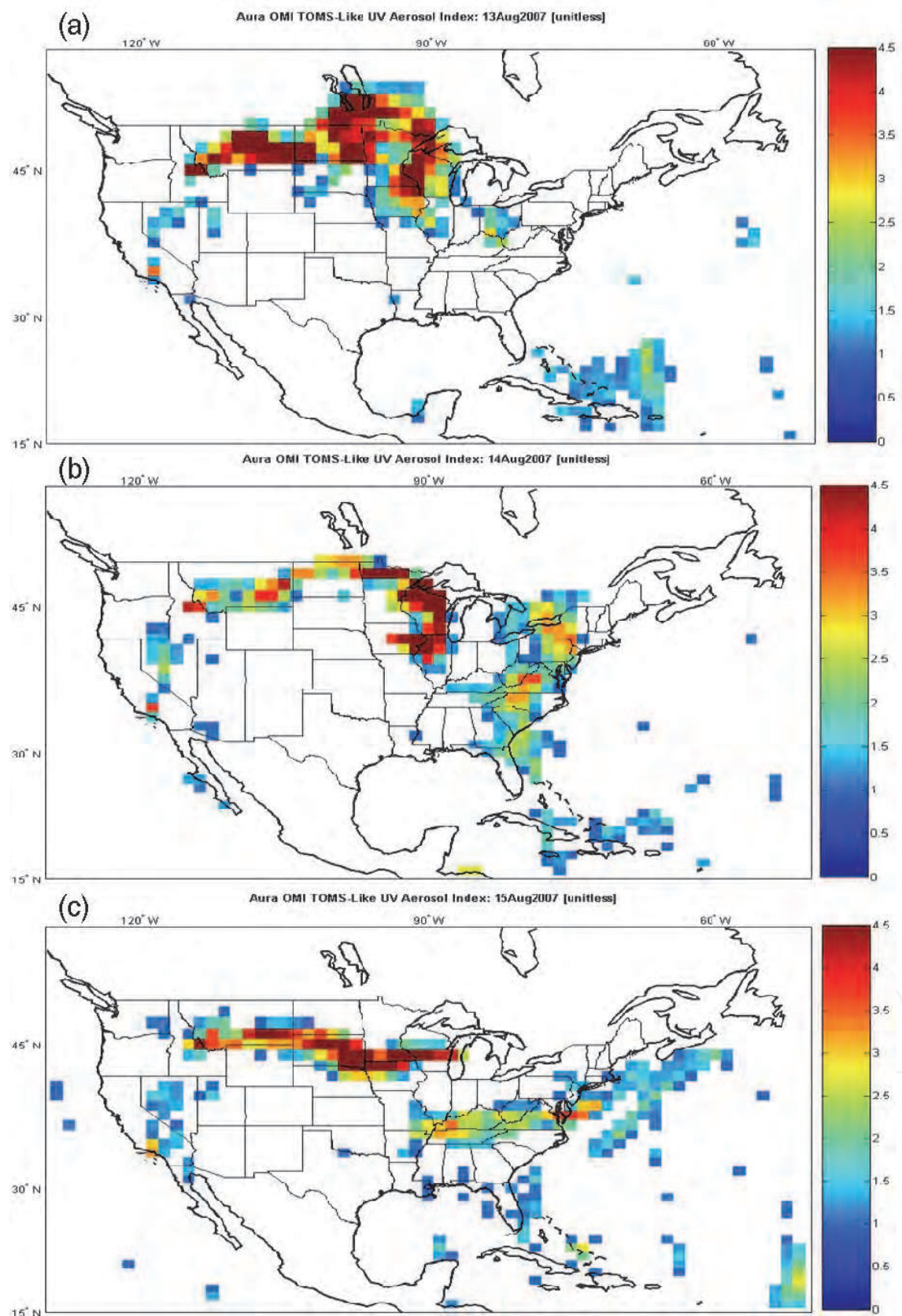


Fig. 18. TOMS OMI UV Aerosol Index for (a) Aug 13, 2007, (b) Aug 14, 2007, (c) Aug 15, 2007 at 354nm.

strongly with native maritime type aerosols, reducing the overall absorbing index. The smoke areas in the OMI imagery of UVAI, was found to coincide well with areas where MODIS (Fig. 17) reported increased aerosol loading compared to its surrounding background. We observe UV Absorbing Index as high as 4, which is indicative of highly absorbing aerosols.

We have also examined the biomass nature of the plume directly using the MOPITT Carbon Monoxide (CO) product, which is a good indicator of biomass aerosols and smoke. The results in Fig. 19 show the CO concentrations over the NYC area for the plume event as a function of pressure level. Clear increases in biomass burning are seen on Aug 14 and 15, marked by the increase in CO concentrations. Note however, that little difference in CO concentration is seen between the 14th and 15th due to the inability of the satellite sensor to see to the PBL layer.

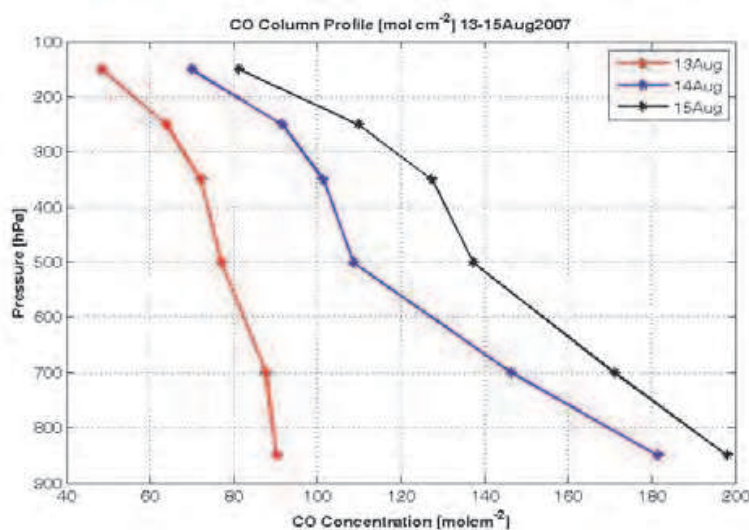


Fig. 19. MOPITT column profile of carbon monoxide concentration of Aug 13-15, 2007 at six pressure levels: 850, 700, 500, 350, 250, and 150 hpa.

7.2 Plume transport using geostationary satellites

In all the previous observations, the satellites were polar orbiting so very few observations can be made daily. However, geostationary observations can be used to explore transport of pollution with high temporal resolution. In fact, the GOES Aerosol and Smoke product (GASP) provides aerosol optical depth retrievals over the United States at 4 km spatial resolution and 30 minutes intervals (Prados et al., 2007; Knapp et al., 2002a, 2002b, 2005). Retrievals are performed over land and ocean providing a full view of the earth daily. The GOES AOD retrieval method uses the visible channel of the GOES-12 Imager data to retrieve aerosol information. The GOES retrieval method is a three-step process. First, a background image composite is created of the visible imagery for each satellite observation time, using the visible image from the past 28 days including the current image. The second minimum reflectance (second darkest pixel) is selected and used in the background composite. Secondly, an atmospheric correction is applied and the Radiative Transfer (RT) model, which assumes a continental aerosol model from the Look Up Table (LUT) generated with the 6S RT model, is used to connect the top of the atmosphere (TOA) reflectance to a surface reflectance. In the final step, the calculated surface reflectance, the LUT, and the

GOES visible image are used to retrieve the aerosol optical depth at 550 nm (Prados et al., 2007; Knapp et al., 2002a, 2002b, 2005). Since the GASP product must assume an aerosol type (background continental), it may be thought that the AOD might be quite inaccurate when applied to smoke. However, the GOES visible channel is fairly insensitive to absorbing effects and since the particle size distributions are quite compatible, we might expect fairly good quantitative measures of AOD.

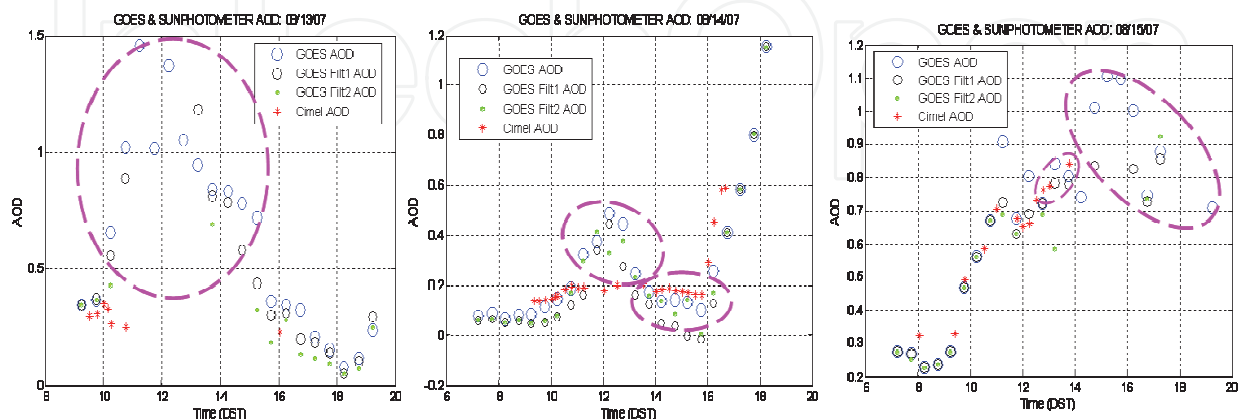


Fig. 20. Comparison of the AERONET sun-photometer (Cimel) derived AOD and GASP AOD products at CCNY on Aug 13-15, 2007

In Fig. 20 we show a comparison of the AERONET sun-photometer derived AOD and GASP AOD products at CCNY for Aug 13-15, 2007. The GASP pixel was centered over CCNY and the AOD was averaged over a $0.1^\circ \times 0.1^\circ$ grid for every 30 minutes of data. Although the GASP product uses a single channel, we still see excellent temporal agreement between the GASP AOD and the sun-photometer AOD product when both data sets exist. However, the GASP measurements are often given when the sky radiometer measurements are not available. These gaps in the sun-photometer data exist due to the presence of clouds in the instruments field of view, where an automated cloud-screening algorithm has been applied. In the original formulation, the GASP AOD has not been properly cloud screened, and therefore, a high optical depth value due to broken clouds is observed, as indicated by the circled regions in Fig. 20. However, when applying a more conservative cloud screening technique to the GOES data (courtesy of NOAA/STAR team), most of the cloud pixels were removed while still leaving the plume AOD measurements unaffected.

7.3 Evaluation of the plume vertical structure using active lidar and passive radiometry

The CCNY lidar co-located with a CIMEL sun-photometer is available for extensive ground measurements. Lidar measurements of the smoke event from Aug 13 to 15 are illustrated in Fig. 21. (a) shows that on Aug 13, we observe prior to the smoke plume arrival over NYC, a clear atmosphere above CCNY with no visible evidence of plumes aloft. On Aug 14, the vertical profile retrieved by the lidar shows a distinct aerosol layer, identified by its strong aerosol backscatter in the late afternoon at about 7 km altitude in Fig. 21 (b). However, by the following day (Aug 15), as the boundary layer developed and the smoke plumes continued to pollute the free troposphere over CCNY, the most noticeable impact of the smoke was its downward advection and mixing with the boundary layer by 14:00 EST.

In examining the spatial extent of the vertical plume structure, we also looked at the NASA Micro-Pulse Lidar NETwork (MPLNET) for simultaneous measurement with the CCNY lidar. The MPLNET operates a lidar at GSFC (39° N, 76° W), downwind from the CCNY lidar, which also has a collocated sun-photometer instrument. Fig. 22 displays the MPLNET/NASA Goddard Space Flight Center Micro Pulse Lidar normalized relative backscatter ratios measured on 14-15 August, the same days as CCNY lidar observations. In Fig. 22, we can see smoke plumes between 3 and 10 km on Aug 14 and between 2 and 6 km on Aug 15, similar to that observed over the CCNY site, with the exception that the Aug 14 plumes over GSFC had already begun descent, although no boundary layer mixing was evident. Backward trajectories ending at GSFC also showed similar air parcel patterns from the source as that ending at CCNY. It is also important to highlight the fact that the boundary layer mixing on Aug 15 occurred about the same time (14:00 EST) at both locations, which is consistent with the HYSPLIT trajectory analysis.

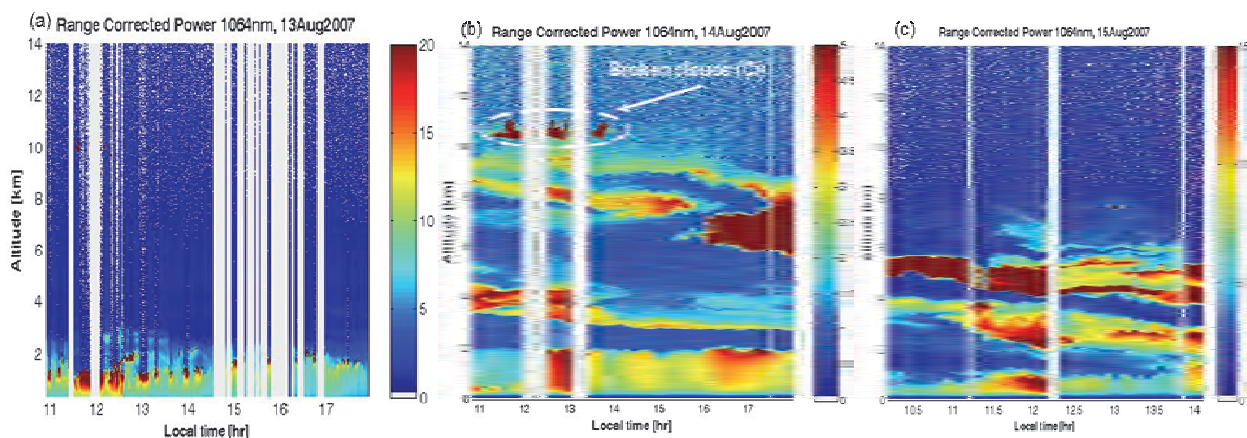


Fig. 21. CCNY range corrected lidar returns at 1064nm showing high altitude plume formation from Idaho, Montana, and Wyoming fires. a) Aug 13: before evidence of smoke plume arrival to NYC b) Aug 14: onset of plumes with lofted layer and no evidence of PBL interactions c) Aug 15: plumes advect downwards interacting with PBL.

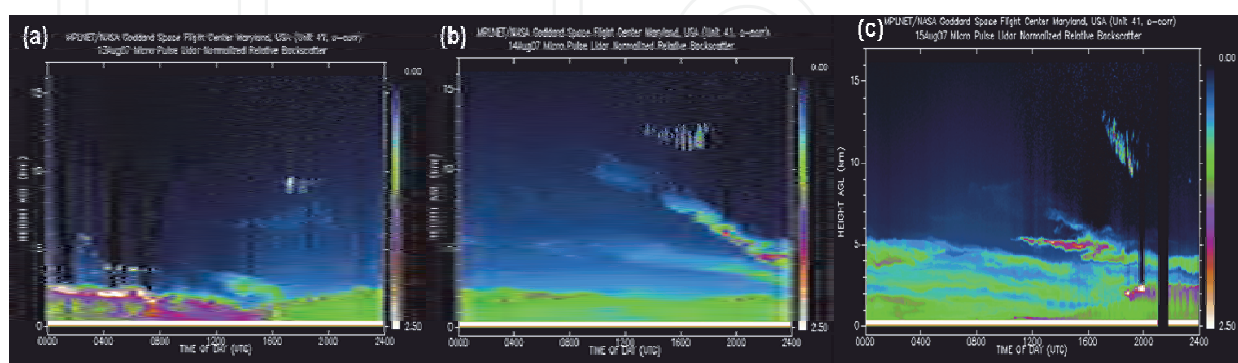


Fig. 22. MPLNET/NASA Goddard Space Flight Center Micro Pulse Lidar normalized relative backscatter ratios measured on (a) Aug 13 before the onset of the smoke plumes, (b) Aug 14, the onset of the smoke plumes descending towards the boundary layer but no visible mixing, and (c) Aug 15, plume advected downwards and mixed with the surface air.

7.4 Plume properties and identification

Unlike the MPLNET, the CCNY lidar has multi-wavelength capabilities allowing us to look for spectral characteristics of the aerosol useful for identification. For example, the plume angstrom coefficient derived from the lidar backscatter measurements as a function of altitude, which we define as:

$$\beta_{aer}(\lambda_1, \lambda_2) = C\lambda^{-\alpha(\lambda_1, \lambda_2)} \quad (5)$$

where C is an arbitrary constant, β is the aerosol backscatter coefficient, and α is the angstrom exponent can help distinguish between small smoke particles and large dust particles in an aloft plume. In doing this calculation, care must be made that channels are calibrated. The 532 nm channel is calibrated based on clear molecular reference signals but the 1064 nm channel requires more care since the molecular reference at 1064 nm channel is too weak. To do this, we employed (Gan et al., 2008; Wu et al., 2010) a cloud base calibration method which results in accuracies $\sim 15\%$. In Fig. 24 (c) we note that the plume has a large (~ 2) and stable angstrom exponent as a function of altitude, which is a

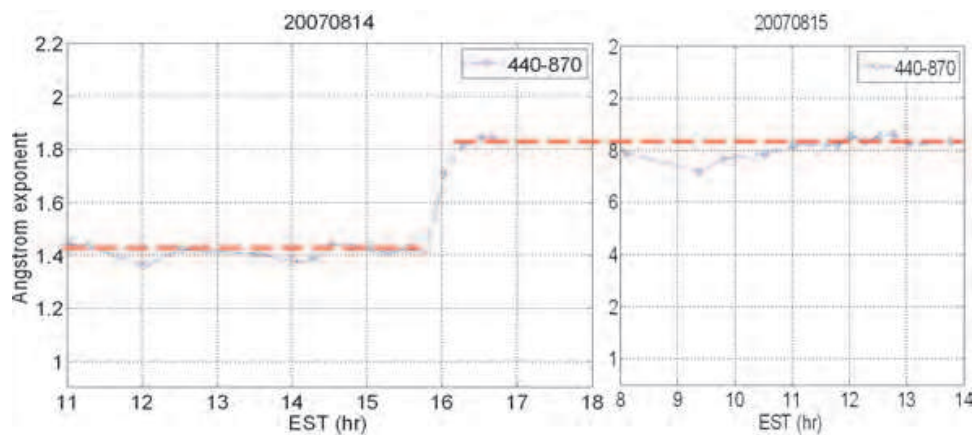


Fig. 23. Column integrated angstrom coefficient derived from sun photometer AOD measurements using 440 – 870 nm channels.

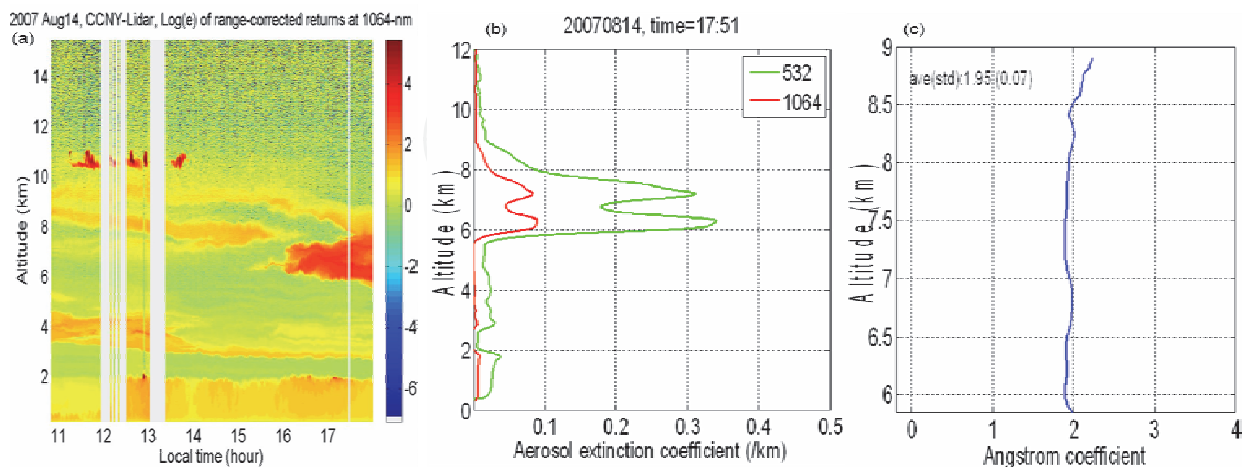


Fig. 24. (a) Lidar range corrected power at 1064 nm, (b) Extinction coefficient obtained from lidar at 17:51 EST, (c) Angstrom coefficient (unitless) using two wavelengths obtained using Equation 5.

clear indication of small particles. These results are reinforced when the sky radiometer angstrom coefficient is calculated, as illustrated in Fig. 23. In particular, we note changes in the angstrom signature (increasing from 1.4 to 1.8 by late afternoon on Aug 14) indicating an increase of fine mode particulates entering the air column. Furthermore, the angstrom coefficients remained fairly constant and stable over the entire 2-days episode, indicating that we are dealing with the same type of particulates, not necessarily coming from a single source. These results are also in good quantitative agreement with the CCNY lidar derived angstrom coefficients.

7.5 Smoke influence on local air quality

We have already noted the advection of the plume into the PBL, so it is natural to explore any ground signatures that indicates an increase in air pollution in the PBL. Fig. 25 shows the near surface particulate loadings on August 13-14 obtained from the NYSDEC. On Aug 14, as expected, the PM_{2.5} loadings were low. These observations showed no evidence of boundary layer interaction with upper troposphere plumes, and at the surface scattering coefficients and particulate loadings remained low, which is a characteristic of clear and relatively unpolluted air within the boundary layer. On the other hand, by the afternoon of Aug 15, there was a large-scale descent of smoke plumes, resulting in a significant increase in the surface PM_{2.5} loadings, compared to the state prior to plume interaction. What is interesting is that the semi-empirical relation between PM_{2.5} and column AOD assuming a well mixed PBL layer (Zhang et al., 2009) Equation 1 would lead to dramatically large overestimates of the surface pollution. However, by using the lidar extinction, we can quantify the AOD of the plume and subtract that contribution from the GOES satellite. The resulting matchup is much improved (Fig. 25) even when the plume interacts with the PBL resulting in tangible increases in the PM_{2.5} concentration.

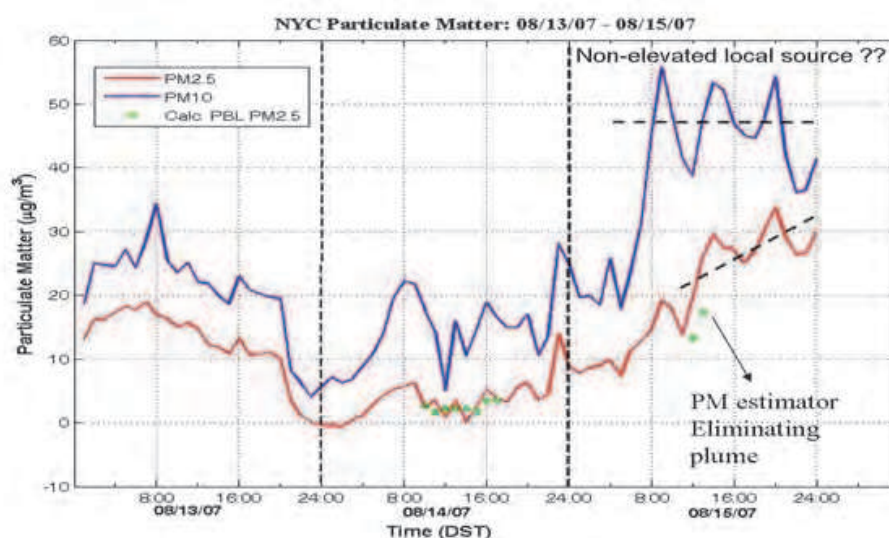


Fig. 25. Ground level PM_{2.5} and PM₁₀ surface loadings for NYC on Aug 13-15, 2007.

8. Summary

To summarize, the use of vertical profiling sensors has found multiple applications in improving our understanding of pollution and transport processes. In this chapter, we show

not only the importance of remote sensing instruments in monitoring the vertical distribution of air quality but also demonstrate how they can unravel difficulties in air quality retrieval from satellite techniques.

We first illustrate that current meteorological forecast models can reliably determine the PBL height even in urban environments in cases where convective heating is the dominant mechanism. We find in such cases correlations ($R > 0.85$) occur although some over biases are observed in the non-local (BLK and ACM2) schemes. In making these comparisons, the use of the Wavelet Covariance Transform (WCT) method to analyze the lidar profiles together with additional constraints was important in isolating the convective layer from residual and plume layers. In addition, eyesafe 24 hour / 7 days ceilometer measurements were used to understand the most critical anomalies in the CMAQ PM_{2.5} forecasts. Using the vertical information, the over biases are shown to be most attributable to CMAQ forcing the pollution too near the surface and less to errors in the emission inventories.

Finally, satellite and active sensors were used to demonstrate how long distance plume transport events can affect local pollution including clear observation of how plumes can advect into the PBL and enhance local PM_{2.5} surface concentrations. Although forest fires are basically local phenomena, they can also contribute to changes of the atmosphere on a regional or even global scale by generating large amounts of aerosol particles, which can be transported over large distances. Therefore, our analysis of the transport of the Idaho and Montana forest fire plumes over the eastern United States during Aug 2007, demonstrates the importance of pollution monitoring and prediction. In particular, we find direct evidence that even long term transport of lofted plume layers can mix with PBL modifying the surface level air-quality

9. Acknowledgment

This chapter is partially supported by NOAA-CREST #NA17AE1625 and NOAA-ISET #NA06OAR4810187. The views, opinions and findings contained in this report are those of the author(s) and should not be construed as an official NOAA or U.S. Government position, policy, or decision. The authors greatly appreciate datasets and helpful advice that were supplied by Jia-Yeong Ku from NYSDEC.

10. References

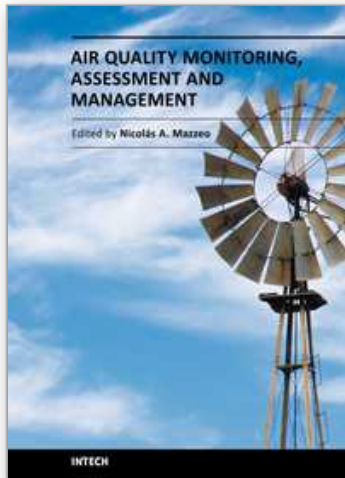
- Anderson, J. R., Hardy, E. E., Roach, J. T., & Witmer, R. E. (1976). A Land Use And Land Cover Classification System For Use With Remote Sensor Data, USGS Geological Survey Professional Paper 964.
- Atkinson, B. W. (2003) Numerical modeling of urban heat-island intensity, *Bound.-Layer Meteor.*, 113, 285–310.
- Baar, H., Ansmann, A., Engelmann, R. and Althausen, D. (2008). Continuous monitoring of the boundary-layer top with lidar. *Atmos. Chem. Phys. Discuss.*, 8, 10749-10790.
- Baker, D., Downs, T., Ku, M., Hao, W., Sistla, G., Kiss, M., Johnson, M. and Brown, D. (2009). Sensitivity Testing of WRF Physics Parameterizations for Meteorological Modeling and Protocol in Support of Regional SIP Air Quality Modeling in the OTR Ozone Transport Commission Modeling Committee.

- Braak, R., Torres, O., Veihelmann, B., Veeffkin, J. P., Kroon, M. and Levelt, P. (2007). OMI UV absorbing index as a tracer for transport of Australian biomass burning aerosols', *Geophys. Res. Abstracts*, 9.
- Brooks, I. M. (2003). Finding Boundary Layer Top: Application of a Wavelet Covariance Transform to Lidar Backscatter Profiles, *J. Atmospheric & Oceanic Technology*, Vol. 20, 1092-1105.
- Davis, K. J., Gamage, N., Hagelberg, C. R., Kiemle, C., Lenschow, D. H. & Sullivan, P. P., (2000). An Objective Method for Deriving Atmospheric Structure from Airborne Lidar Observations, *J. Atmospheric & Oceanic Technology*, Vol. 17, 1455-1468.
- DeMott, P. J., Sassen, K., Poellot, M. R., Baumgardner, D., Rogers, D. C., Brooks, S. D., Prenni, A. J. and Kreidenweis, S. M. (2003). African dust aerosols as atmospheric ice nuclei, *Geophysical Research Letters*, Vol. 30, No. 14, 1732, doi:10.1029/2003GL017410
- Doraiswamy, P., Hogrefe, C., Hao, W., Civerolo, K., Ku, J.Y. & Sistla, G. (2010). A Retrospective Comparison of Model-Based Forecasted PM_{2.5} Concentrations with Measurements, *J. Air & Waste Manage. Assoc.* 60(11):1293-308.
- Dockery, D.W., Speizer, F.E., Stram, D.O., Ware, J.H., Spengler, J.D. and Ferris, B.G. Jr. (1989). Effects of inhalable particles on respiratory health of children *Am. Rev. Respir. Dis.*; (United States); Journal Volume: 139:3 Pages: 587-594
- Emeis, S., Schafer, K. & Munkel, C. (2008). Surface-based Remote Sensing of the Mixing-Layer Height - a review, *Meteorological Zeitschrift*, Vol. 17, No. 5, 621-630.
- EPA (1999a). User Manual for the EPA Third-Generation Air Quality Modeling System (Models-3Version 3.0), EPA-600/R-99/055, pp.1-1-1-18, United States Environmental Protection Agency.
- EPA (1999b). Science Algorithms of the EPA Models-3Community Multiscale Air Quality (CMAQ) Modeling System, PART II: Chapters 9-18, EPA-600/R-99/030, pp. 10-1 - 10-23, United States Environmental Protection Agency.
- Eresmaa, N., Karppinen, A., Joffre, S. M., Rasanen, J. and Talvitie, H. (2006). Mixing height determination by ceilometer, *Atmos. Chem. Phys.*, 6, 1485-1493.
- Flagg, D., & Taylor, P. A. (2008). Sensitivity Morphology in Urban Boundary Layer Modeling at the Mesoscale, *AMS 18th Symposium on Boundary Layers and Turbulence*, 7A.3.
- Gamage, N. & Hagelberg, C. (1993). Detection and analysis of microfronts and associated coherent events using localized transform, *J. Atmos. Sci*, 50, 750-756.
- Gan, C. M., Charles, L., Gross, B., Moshary, F. and Ahmed, S. (2008). Analysis of the interaction of aerosol transport layers on local air quality, *IGARSS IEEE International Vol.4*.
- Gan, C. M., Wu, Y., Gross, B., and Moshary, F. (2011). Application of Active Optical Sensors to Probe the Vertical Structure of the Urban Boundary Layer and Assess Anomalies in Air Quality Model PM_{2.5} Forecasts, To appear *Atmos. Environ.*
- Girardot, S. P.(2006). Characterization of ambient ozone and fine particulate matter (PM_{2.5}) concentrations, human exposure, and pulmonary health effects in the Great Smoky Mountains National Park, EMORY UNIVERSITY, Thesis ID 3212358

- Haij, de, M.J., Wauben, W.M.F., Klein Baltink, H. and Apituley, A. (2009). Determination of the mixing layer height by a ceilometer *Proceedings of the 8th International Symposium on Tropospheric Profiling*, ISBN 978-90-6960-233-2 Delft, The Netherlands.
- Hennemuth, B., & Lammert, A. (2006). Determination of the atmospheric boundary layer height from radiosonde and lidar backscatter, *Boundary-Layer Meteorology* 120: 181-200
- Herman, J. R., Bhartia, P. K., Torres, O., Hsu, C., Seftor, C. and Celarier, E. (1997). Global distribution of UV absorbing aerosols from Nimbus 7/TOMS data. *J. Geophys. Res.* 102, 16,911-16,922.
- Hondula, D. M., Sitka, L., Davis, R. E., Knight, D. B., Gawtry, S. D., Deaton, M. L., Lee, T. R., Normile, C. P. and Stengera, P. J. (2009). A back-trajectory and air mass climatology for the Northern Shenandoah Valley, USA, *Int. J. Climatol.* DOI: 10.1002/joc.1896
- Hong, S.Y., Noh, Y. & Dudhia, J. (2006). A New Vertical Diffusion Package with an Explicit Treatment of Entrainment Processes, *Mon. Wea. Rev.*, 134, 2318-234.
- Janjić, Z.I. (1990). The step-mountain coordinate: physical package. *Mon. Wea. Rev.*, 118, 1429-1443.
- Janjić, Z.I. (1994). The step-mountain eta coordinate model: further developments of the convection, viscous sublayer and turbulence closure schemes. *Mon. Wea. Rev.*, 122, 927-945.
- Janjić, Z.I. (2001) Nonsingular Implementation of the Mellor-Yamada Level 2.5 Scheme in the NCEP Meso model, National Centers for Environmental Prediction, Office Note #437
- Jiang, W., Smyth, S., Giroux, E., Rothand, H. & Yin, D. (2006). Differences between CMAQ fine mode particle and PM_{2.5} concentrations and their impact on model performance evaluation in the lower Fraser valley, *Atmospheric Environment*, 40, 4973-4985.
- Jorba, O., Pe' Rez, C., Rocadenbosch, F. and Baldasano, J. M. (2004). Cluster Analysis of 4-Day Back Trajectories Arriving in the Barcelona Area, Spain, from 1997 to 2002, *Journal of Applied Meteorology* Vol. 43 pp. 887-901
- Kaufman, Y. J. (1993). Aerosol optical thickness and atmospheric path radiance, *J. Geophys. Res.*, 98(D2), 2677-2692.
- Knapp, K. R. (2002a). Quantification of aerosol signal in GOES 8 visible imagery over the United States, *J. Geophys. Res.*, VOL. 107, NO. D20.
- Knapp, K. R., Vonder Haar, T. H. and Kaufman, Y. J. (2002b). Aerosol Optical Depth Retrieval from GOES-8: Uncertainty study and Retrieval validation over South America, *J. Geophys. Res.*, VOL. 107, NO. D7.
- Knapp, K. R., Frouin, R., Kondragunta, S. and Prados, A. (2005). Towards Aerosol Optical Depth Retrievals over land from GOES visible radiances: determine surface reflectance, *International Journal of Remote Sensing*, VOL. 26, NO. 18.
- Koji, M. and Lovei, M. (2001). Urban Air Quality Management Coordinating Transport, Environment and Energy Policies in Developing Countries, World Bank Technical paper No. 508.
- Kovalev, V.A. & Eichinger, W.E. (2004). *Elastic Lidar: Theory, Practice, and Analysis Methods*, Wiley-Interscience, USA.

- Liu, Y., Chen, F., Warner, T., & Basara, J. (2006). Verification of a Mesoscale Data-Assimilation and Forecasting System for the Oklahoma City Area During the Joint Urban 2003 Field Project, *J. Appl. Meteor.*, 45, 912-929.
- Malm, W.C., Sisler, J.F., Huffman, D., Eldred, R.A. & Cahill, T.A. (1994). Spatial and seasonal trends in particle concentration and optical extinction in the United States, *Journal of Geophysical Research-Atmospheres* 99 (D1) (1994), pp. 1347-1370.
- Mellor, G.L. and T. Yamada (1982). Development of a turbulence closure model for geophysical fluid problems. *Rev. Geophys. Space Phys.*, 20, 851-875.
- Mestayer, P.G., Durand, P., Augustin, P., Bastin, S., Bonnefond, J. M., Benech, B., Campistron, B., Coppalle, A., Delbarre, H. and Dousset, B. et al. (2005) The urban boundary layer field campaign in Marseille (UBL/CLU-ESCOMPTE): Set-up and first results, *Boundary-Layer Meteor.*, 114: 315-365.
- Otte, T. L. (2008a). The impact of nudging in the meteorological model for retrospective air quality simulations. Part I: Evaluation against national observation networks, *J. Appl. Meteor. Climatol.*, 47, 1853-1867.
- Otte, T. L. (2008b) The impact of nudging in the meteorological model for retrospective air quality simulations. Part II: Evaluating collocated meteorological and air quality observations", *J. Appl. Meteor. Climatol.*, 47, 1868-1887.
- Piringer, M. et al. (2007). The surface energy balance and the mixing height in urban areas - activities and recommendations of COST-Action 715, *Boundary-Layer Meteor.* 124:3-24.
- Pleim, J. E. & Gilliam, R. (2009). An indirect data assimilation scheme for deep soil temperature in the Pleim-Xiu land surface model, *J. Appl. Meteor. Climatol.*, 48, 1362-1376.
- Prados, A.I., Kondragunta, S., Ciren, P. and Knapp, K. R. (2007). GOES Aerosol/Smoke Product (GASP) over North America: Comparisons to AERONET and MODIS observations, *J. Geophys. Res.* 112.
- Skamarock, W. C. et al. (2008). A Description of the Advanced Research WRF Version 3, NCAR TECHNICAL NOTE NCAR/TN-475+STR.
- Stull, R.B. (1988). *An Introduction to Boundary Layer Meteorology*, Kluwer Academic Publishers, Dordrecht/Boston/London.
- Taha, H. (1999) Modifying a mesoscale meteorological model to better incorporate urban heat storage: A bulk-parameterization approach, *J. Appl. Meteor.*, 38, 466-473.
- Torres, O., Decaie, R., Veefkind, P. and G. de Leeuw (2002). OMI Aerosol Retrieval Algorithm, OMI Algorithm Theoretical Basis Document, Volume III, Version 2.
- Wu, Y., Chaw, S., Gross, B., Moshary, F. & Ahmed, S. (2009). Low and optically thin cloud measurements using a Raman-Mie lidar, *Appl. Opt.* 48, 1218-1227.
- Wu, Y, Gan, C. M., Gross, B., Moshary, F. and Ahmed, S. (2010). Calibration of lidar at 1064-nm channel using the water-phase and cirrus clouds, To Appear *Applied Optics*.
- Zhang, H., Hoff, R.M. and Engel-Cox, J.A. (2009). The relation between Moderate Resolution Imaging Spectroradiometer (MODIS) aerosol optical depth and PM_{2.5} over the United States: a geographical comparison by EPA regions, *J. Air & Waste Manage. Assoc.*, 59, 1358-1369.

- Zhao, Y. and Frey, H. C. (2004). Development of Probabilistic Emission Inventory of Selected Air Toxics for an Urban Area, Air & Waste Management Association, Pittsburgh, PA.
- Arrau, C. P. & Peña, M. A. (2010). Urban Heat Island Causes, In: *Home Urban Heat Island Effect*, 03.10.2011, Available from: <http://www.urbanheatlands.com/home>
- Voogt, J. A. (2004). Urban Heat Islands: Hotter Cities, In: *ActionBioscience.org*, 03.10.2011, Available from: <http://www.actionbioscience.org/environment/voogt.html#primer>



Air Quality Monitoring, Assessment and Management

Edited by Dr. Nicolas Mazzeo

ISBN 978-953-307-317-0

Hard cover, 378 pages

Publisher InTech

Published online 08, July, 2011

Published in print edition July, 2011

Human beings need to breathe oxygen diluted in certain quantity of inert gas for living. In the atmosphere, there is a gas mixture of, mainly, oxygen and nitrogen, in appropriate proportions. However, the air also contains other gases, vapours and aerosols that humans incorporate when breathing and whose composition and concentration vary spatially. Some of these are physiologically inert. Air pollution has become a problem of major concern in the last few decades as it has caused negative effects on human health, nature and properties. This book presents the results of research studies carried out by international researchers in seventeen chapters which can be grouped into two main sections: a) air quality monitoring and b) air quality assessment and management, and serves as a source of material for all those involved in the field, whether as a student, scientific researcher, industrialist, consultant, or government agency with responsibility in this area.

How to reference

In order to correctly reference this scholarly work, feel free to copy and paste the following:

Chuen Meei Gan, Barry Gross, YongHua Wu and Fred Moshary (2011). Application of Remote Sensing Instrument in Air Quality Monitoring, Air Quality Monitoring, Assessment and Management, Dr. Nicolas Mazzeo (Ed.), ISBN: 978-953-307-317-0, InTech, Available from: <http://www.intechopen.com/books/air-quality-monitoring-assessment-and-management/application-of-remote-sensing-instrument-in-air-quality-monitoring>

INTECH
open science | open minds

InTech Europe

University Campus STeP Ri
Slavka Krautzeka 83/A
51000 Rijeka, Croatia
Phone: +385 (51) 770 447
Fax: +385 (51) 686 166
www.intechopen.com

InTech China

Unit 405, Office Block, Hotel Equatorial Shanghai
No.65, Yan An Road (West), Shanghai, 200040, China
中国上海市延安西路65号上海国际贵都大饭店办公楼405单元
Phone: +86-21-62489820
Fax: +86-21-62489821

© 2011 The Author(s). Licensee IntechOpen. This chapter is distributed under the terms of the [Creative Commons Attribution-NonCommercial-ShareAlike-3.0 License](https://creativecommons.org/licenses/by-nc-sa/3.0/), which permits use, distribution and reproduction for non-commercial purposes, provided the original is properly cited and derivative works building on this content are distributed under the same license.

IntechOpen

IntechOpen